ACS NANO

www.acsnano.org

ARTICLE

Physical Regimes and Mechanisms of Picosecond Laser Fragmentation of Gold Nanoparticles in Water from X-ray Probing and Atomistic Simulations

Anton Plech, Meike Tack, Hao Huang, Mikhail Arefev, Anna R. Ziefuss, Matteo Levantino, Hasan Karadas, Chaobo Chen, Leonid V. Zhigilei, and Sven Reichenberger*

Cite This: *ACS Nano* 2024, 18, 10527−10541

Read Online

ACCESS | Metrics & More | Article Recommendations | Supporting Information

ABSTRACT: **Laser fragmentation in liquids has emerged as a promising green chemistry technique for changing the size, shape, structure, and phase composition of colloidal nanoparticles, thus tuning their properties to the needs of practical applications. The advancement of this technique requires a solid understanding of the mechanisms of laser−nanoparticle interactions that lead to the fragmentation. While theoretical studies have made impressive practical and mechanistic predictions, their experimental validation is required. Hence, using the picosecond laser fragmentation of Au nanoparticles in water as a model system, the transient melting and fragmentation processes are investigated with a combination of time-resolved X-ray probing and atomistic simulations. The direct comparison of the diffraction profiles predicted in the simulations and measured in experiments has revealed a sequence of several nonequilibrium processes triggered by the laser irradiation. At low laser fluences, in the regime of nanoparticle melting and resolidification, the results provide evidence of a transient superheating of crystalline nanoparticles above the melting temperature. At fluences about three times the melting threshold, the fragmentation starts with evaporation of Au atoms and their condensation into small satellite nanoparticles. As fluence increases above five times the melting threshold, a transition to a rapid (explosive) phase decomposition of superheated nanoparticles into small liquid droplets and vapor phase atoms is observed. The transition to the phase explosion fragmentation regime is signified by prominent changes in the small-angle X-ray scattering profiles measured in experiments and calculated in simulations. The good match between the experimental and computational diffraction profiles gives credence to the physical picture of the cascade of thermal fragmentation regimes revealed in the simulations and demonstrates the high promise of the joint tightly integrated computational and experimental efforts.**

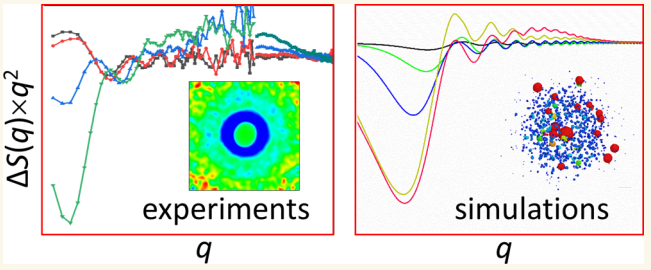

KEYWORDS: *laser fragmentation in liquid, nanoparticles, nanoclusters, phase explosion, time-resolved X-ray scattering, molecular dynamics simulations*

INTRODUCTION

The synthesis of surfactant-free nanoparticles (NPs) by pulsed laser synthesis and processing of colloids (LSPC) has significantly impacted several research fields, such as biomedicine,[1,2] additive manufacturing,[3,4] and catalysis.[5−7] The advantage of LSPC over conventional nanoparticle synthesis strategies is the use of photons for material processing, which not only enables the synthesis of nanoparticles with high purity and 100% atom yield[8,9] but also conceptually enables a truly green and renewable synthesis of nanomaterials once the lasers are operated solely with renewable electrical power. Throughout the last two decades, pulsed laser ablation in liquid (PLAL) has been the dominant LSPC method of NP synthesis experiencing steady growth in productivity, broadening of material systems, and expanding the range of applications utilizing the NPs.[9−12] The method is not free of drawbacks, which include the limited size control

Received: December 7, 2023
Revised: March 13, 2024
Accepted: March 20, 2024
Published: April 3, 2024

ACS Publications © 2024 American Chemical Society

https://doi.org/10.1021/acsnano.3c12314
ACS Nano 2024, 18, 10527−10541

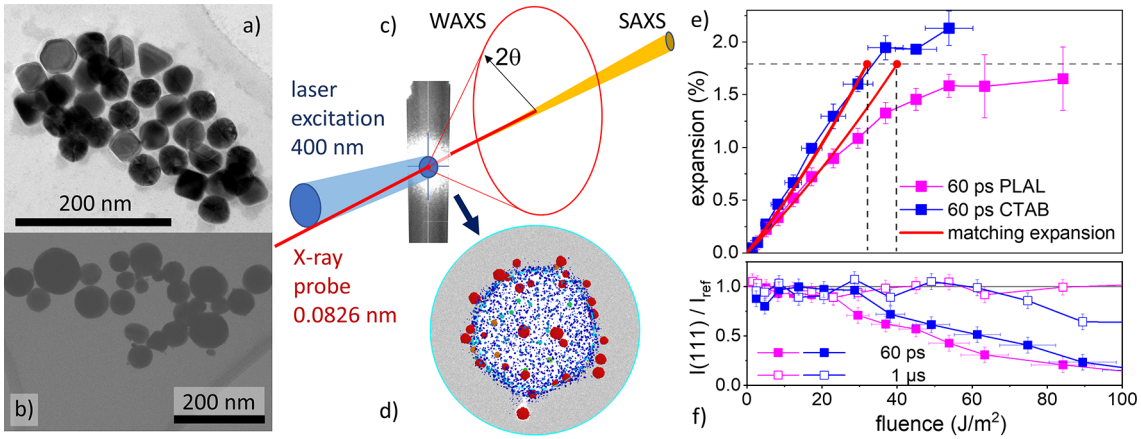

Figure 1. General overview of the experiment: the colloid containing gold NPs produced by seeded chemical synthesis (TEM micrograph in panel a) or laser ablation (TEM micrograph in panel b) is exposed to an excitation laser pulse and an X-ray probe pulse through a vertical cylindrical jet (panel c) and recorded by a detector at different distances (SAXS and WAXS). The interpretation of the experimental data is assisted by the comparison to the results of atomistic simulations, as exemplified in panel d. The WAXS observables include the positions and intensities of the (111) powder diffraction peak, as illustrated in panels e and f, respectively. The lattice expansion evaluated from the shift of the (111) peak at a delay of 60 ps (panel e) is interpreted in terms of the NP heating and partial melting (see text). The red lines are the result of fitting of eqs 1 and 2 to data obtained for CTAB and PLAL NPs. This fitting is also used to define the corresponding fluence thresholds, F_0^{CTAB} and F_0^{PLAL}, for heating the NPs up to the melting temperature T_m. The values of F_0 and the lattice expansion at T_m are marked in panel e by the vertical and horizontal dashed lines, respectively. The laser-induced changes in the (111) peak intensity at 60 ps and 1 μs delays are shown in panel f by solid and open symbols, respectively.

and polydispersity of the colloids produced by PLAL.[13−15] The latter has been shown to be rooted in the complex hierarchical nature of the ablation process and the coexistence of different mechanisms of the NP generation in PLAL.[15−20]

The limitations of PLAL have led to the development of a complementary technique dubbed laser fragmentation in liquid (LFL),[21−24] where larger NPs are fragmented to produce a population of smaller NPs with a desired narrow size distribution. Notably, LFL has successfully pushed the size limit of the accessible NPs below 5 nm,[23−27] which is hardly accessible to PLAL.[6,9,12] Further advancing the LFL technique for tailoring the sizes, shapes, defect structures, phase compositions, and morphologies of the NPs to the needs of practical applications requires a solid understanding of the mechanisms of laser−NP interactions leading to the fragmentation.

The fragmentation mechanisms discussed in the literature can be separated into photothermal, photomechanical, and electrostatic ones. The thermal fragmentation mechanism was first discussed in terms of quasi-equilibrium processes, where the particle thermodynamic state follows the binodal of solid−gas to liquid−gas coexistence, and the NP size reduction proceeds through evaporation[28] and condensation of the evaporated atoms into small clusters.[21] However, it becomes clear that evaporation rates are not sufficient to keep up with the rapid heating of colloidal NPs excited by femtosecond to nanosecond laser pulses. At sufficiently high levels of excitation, the NPs can be superheated up to the limit of thermodynamic stability of the molten material (close to the spinodal temperature), leading to the so-called "phase explosion," i.e., a rapid spontaneous decomposition into vapor and liquid droplets.[29,30] The transition to the phase explosion regime of LFL has been predicted computationally[31−33] and supported by experimental observations of bimodal size distributions of fragmentation products.[24,34−36]

The photomechanical processes can also contribute to the NP fragmentation, particularly under conditions of stress confinement,[37,38] when the NP heating time is shorter than the time required for the thermoelastic relaxation, i.e., expansion of the NP. While the conditions for photomechanical fragmentation are more readily satisfied in laser interactions with molecular and oxide particles,[27,39−43] the relaxation of laser-induced stresses may affect the dynamics of the thermally driven fragmentation of metal NPs as well.[32,33,44,45] Finally, nonthermal processes related to the local near-field enhancement of the laser light intensity may also contribute to the femtosecond laser fragmentation of NPs through nonthermal (and directional) electron and ion emission, strong charging of NPs, and subsequent Coulomb instability.[46−50] These effects are typically amplified in close-to-resonant excitation, such as the plasmon resonance in several metallic systems. The complexity of the multiscale intertwined processes involved in LFL makes it difficult to establish clear maps of the laser fluence/intensity fragmentation regimes and mechanisms. There are also open questions on the role of secondary processes, such as melting and resolidification, generation and collapse of nanobubbles around the irradiated NPs, and the heat transfer from the NPs to the liquid environment.

Steady advances in the time-resolved X-ray[36,51−53] and optical probing[54−56] of the dynamics of nanobubbles as well as the evolution of sizes and crystallinity of the fragmentation products[36] have provided important insights into LFL mechanisms. Concurrently, the development of a computational model combining an atomistic molecular dynamics (MD) representation of the NP fragmentation with a continuum treatment of the laser excitation and size-dependent electron−phonon coupling has enabled detailed exploration of the physical regimes and mechanisms of LFL.[32] First applications of the model have revealed the existence of three distinct fluence regimes of LFL of Au NPs defined by an interplay of the phase transformations in the rapidly heated NP (melting, evaporation, phase explosion, and solidification) with the nanobubble dynamics.[32,33] The recent advances in the experimental probing and computational modeling provide an

https://doi.org/10.1021/acsnano.3c12314
ACS Nano 2024, 18, 10527−10541

opportunity to quantitatively map the physical regimes of LFL and link them to the characteristics of the fragmentation products, such as NP sizes, shapes, presence of crystal defects, and phase composition. This endeavor, however, requires direct integration of the computational and experimental efforts.

In the present study, we combine the power of these advanced tools, namely the time-resolved experimental probing and computer modeling of the LFL dynamics. The simulations and experiments are performed for Au NPs irradiated in water by picosecond laser pulses. In the experimental study, Au NPs from chemical synthesis with uniform size distribution are used as a model system. In addition, laser-generated surfactant-free and polycrystalline Au NPs of comparable average size but broader size distribution are used as a representative system with characteristics typical of colloidal NPs produced by PLAL. The fluence threshold for the laser-heated Au NPs to reach the melting temperature is evaluated from the shift of the X-ray powder diffraction (111) peak resolved on the picosecond time-scale using a laser-pump-X-ray-probe setup. This fluence threshold is then used as a reference point for matching the fluence and energy scales in the experiments and simulations. The NP fragmentation regimes are further analyzed in the same setup by comparing the small-angle X-ray scattering (SAXS) profiles measured in experiments at 1 μs after the laser irradiation and calculated for atomic configurations predicted in the simulations. A good agreement in the fluence dependence of the experimental and computational SAXS profiles gives credence to the physical picture of the cascade of thermal fragmentation regimes revealed in the simulations: from the evaporation–condensation at low fluences, to the "mild" phase explosion featuring the reflection of large fragments from the boundary of the nanobubble (inverse Leidenfrost effect) in the medium-fluence regime, and to the "strong" phase explosion leading to a prompt injection of the fragmentation products into water surrounding the nanobubble in the high-fluence regime.

RESULTS AND DISCUSSION

The experimental time-resolved X-ray diffraction probing of the LFL dynamics is performed in this work for two types of initial Au NPs. One type is obtained through seeded chemical synthesis with cetyltrimethylammonium bromide (CTAB) used as a capping agent,[57] yielding mostly single-crystalline faceted NPs (see Figure 1a and larger magnification in Figure S2a) with a relatively narrow mass-weighted size distribution (Figure S1a,c). Another type is generated by picosecond laser ablation in water[24,36,58] followed by fractional centrifugation and stabilization in a NaOH/NaCl solution, as detailed in Methods. The synthesis by PLAL produces mostly spherical NPs (see Figure 1b and larger magnification in Figure S2b) with a broader mass-weighted size distribution (Figure S1b,d). The colloidal NPs are excited (pumped) with single 1 ps laser pulses and probed by 60 ps X-ray pulses (see Figure 1c), all under constant liquid flow conditions.

The computationally assisted mechanistic interpretation of the experimental results is based on predictions of large-scale atomistic simulations of LFL[32,33] (Figure 1d) and is performed in two steps. First, the shift of the crystalline (111) peak in the wide-angle X-ray scattering (WAXS) profiles is used to trace the fluence dependence of the laser heating of NPs up to the melting threshold. Second, using the melting threshold as a reference point for matching the corresponding energy density in the atomistic simulations, the changes in the SAXS profiles with increasing fluence are interpreted in terms of the transitions between several distinct regimes of NP fragmentation predicted in the simulations.

NP Heating and Melting from WAXS Profiles. The processes triggered by laser excitation of NPs below the thresholds for melting and fragmentation are limited to (1) the energy transfer from the excited electrons to the lattice vibrations (electron–phonon coupling),[59] (2) the thermal expansion of NPs, (3) the elastic oscillations of NPs triggered by a combination of the hot-electron pressure and rapid heating of the lattice,[60−65] and (4) the gradual cooling due to the energy transfer to the environment.[66−68] The characteristic time of the electron–phonon equilibration has a strong dependence on the level of excitation,[59,69,70] but it is significantly shorter (<10 ps) than the 60 ps pulse duration of the X-ray probe. As a result, the electron–phonon equilibration occurring within several picoseconds after the laser excitation cannot be resolved with the experimental setup used in the present work. Similarly, tracking the periodic oscillations of the diffraction peak positions due to the laser-induced elastic vibrations of NPs would require much higher temporal resolution,[62−65] as well as a higher size uniformity of the NPs to ensure coherency of the excited vibrational modes. The cooling of the NPs due to the heat transfer to the surrounding water, on the other hand, takes place on a longer time scale of hundreds of picoseconds.[66−68] Therefore, to probe the energy density deposited by the laser pulse through the corresponding lattice expansion, the delay between the laser pulse and the subsequent X-ray probe pulse is set to 60 ps. At this delay time, the electron–phonon coupling is completed, while the heat dissipation into the water environment is still negligible.[68]

The results of the measurements of the lattice expansion performed for both CTAB and PLAL NPs are shown in Figure 1e. To connect the lattice expansion $\Delta a/a_0$ to the incident laser fluence F, we solve the following system of equations describing the increase in temperature T and lattice parameter a in response to the laser energy deposition to a NP with radius R:

$$(1/a)\,\mathrm{d}a = \alpha(T)\,\mathrm{d}T \tag{1}$$

$$\sigma_{\mathrm{abs}}\,\mathrm{d}F = \frac{4}{3}\pi R^3 c_{\mathrm{p}}(T)\,\mathrm{d}T \tag{2}$$

The equations are solved using the temperature-dependent linear coefficient of thermal expansion $\alpha(T)$ and volumetric heat capacity $c_p(T)$ of bulk gold.[71−73] The value of the absorption cross section σ_{abs} is used as a fitting parameter and is chosen to ensure the best description of the experimental data points by eqs 1 and 2. As explained below, all data points up to the presumed melting temperature are used for CTAB NPs, but only the points up to $F < 20$ J/m^2 are used in fitting of the equations to the data measured for PLAL NPs.

The increasing trends exhibited by both $\alpha(T)$ and $c_p(T)$ partially cancel each other, resulting in an almost linear scaling of the thermal expansion with F shown by the red curves in Figure 1e. The value of σ_{abs} produced by fitting of eqs 1 and 2 to the data points for CTAB NPs (nominal diameter of $(2R_i)_{\mathrm{SAXS}}$ = 44 nm, determined via SAXS and in good agreement with TEM analysis in Figure S1) is 3.9×10^{-15} m^2, which is 50% higher than the absorption cross section of 2.54×10^{-15} m^2 predicted by the Mie theory for a 44 nm Au NP

https://doi.org/10.1021/acsnano.3c12314
ACS Nano 2024, 18, 10527−10541

irradiated in water at the same wavelength of 400 nm. The deviation of the effective σ_{abs}, obtained for NPs undergoing rapid laser-induced heating, from the room-temperature Mie theory value is not surprising, as the instantaneous absorption cross section is expected to change during the laser pulse due to the dependence of the electron scattering rate on the lattice and electron temperatures. What is surprising is that a constant (fluence-independent) value of σ_{abs} is providing a reasonable description of the thermal expansion up to the fluence threshold for melting of the NPs. Preliminary calculations combining the solution of the Maxwell equations with two-temperature model description of the electron and lattice temperature evolution in the irradiated NPs suggest that this observation may be explained by a nonmonotonous variation of the transient absorption cross section during the laser pulse. As the electron−electron and electron−phonon scattering rates are increasing during the laser pulse, the optical properties of the NPs get in and out of the plasmon resonance, thus resulting in a weak overall deviation from the linear scaling of the absorbed laser energy with fluence.

The red curves plotted in Figure 1e using eqs 1 and 2 are extended up to the thermal expansion level of 1.79%, which corresponds to the equilibrium melting temperature T_m of the bulk Au.[74,75] The fluence that corresponds to the thermal expansion expected for a NP at T_m is then defined as a reference fluence F_0. The experimental values obtained for the CTAB and PLAL NPs, F_0^{CTAB} = 32 J/m^2 and F_0^{PLAL} = 40 J/m^2, are marked by the vertical dashed lines in Figure 1e. These values of reference fluence can be matched to the corresponding absorbed energy density ε_0 required for heating the NPs up to T_m. It is calculated by integration of $c_p(T)$[71] from 300 K to T_m, giving the value of ε_0 = 29 kJ/mol, or 0.30 eV/atom. As discussed below, the matching of the experimentally obtained values of F_0^{CTAB} and F_0^{PLAL} with ε_0 = 0.30 eV/atom makes it possible to achieve a certain degree of alignment between the experimental fluences and values of the energy density used in the simulations of LFL.

Before moving to the discussion of fragmentation mechanisms, the origin of the deviation of the theoretical curves from the data points in Figure 1e should be addressed. For CTAB NPs, the three data points present above the horizontal dashed line marking the thermal expansion at T_m ($\Delta a/a_0$ = 1.79%) call for an explanation. These data points correspond to fluencies above F_0^{CTAB}; i.e., the energy deposited by the laser pulse is expected to exceed the level required for heating the NPs to T_m. The highest fluence where the crystalline peak with strength/sharpness sufficient for the evaluation of the thermal expansion can still be identified in the WAXS data for CTAB NPs is 54 J/m^2, or 1.69F_0^{CTAB}. The latent heat of melting of bulk gold is ΔH_m = 12.72 kJ/mol, or 0.13 eV/atom. Hence, the energy needed to completely melt a Au NP after heating it to T_m is about 43% of the energy ε_0 needed for reaching the melting temperature.[76,77] Thus, the energy density deposited at a fluence of 1.69F_0^{CTAB} is likely to exceed the energy level required for complete melting of the NPs. The observation that the crystalline peaks are still present at 1.69F_0^{CTAB} can be attributed to the transient survival of some of the crystalline regions in the superheated state. The notion of the transient superheating of the NPs is consistent with the lattice expansion exceeding the level that corresponds to T_m. The extrapolation of $\alpha(T)$ above T_m gives the estimate of 1.12T_m. for a temperature when the lattice expansion $\Delta a/a_0$ would reach the maximum value of 2.12% observed in Figure 1e. This superheating is well below the limit of thermodynamic stability of the crystal lattice against the onset of massive homogeneous nucleation of liquid regions, which was predicted to be ∼1.25T_m for Au.[78,79] The results of recent atomistic simulations of laser melting of 35 nm Au films suggest that the melting process can take up to ∼100 ps at energy densities close to the threshold for complete melting (i.e., at energy densities around $\varepsilon_0 + \Delta H_m$).[78] Thus, the crystalline peaks can indeed be present 60 ps after the laser pulse, when the colloidal solution is probed by the X-ray pulse. At higher fluences, the disappearance of the crystalline peaks is more rapid and occurs prior to the arrival of the probe pulse, as illustrated in Figure S6c in the Supporting Information by the results of a simulation performed for a 20 nm NP and a deposited energy density of 1.7ε_0.

For the PLAL NPs, the data points in Figure 1e exhibit a significantly weaker fluence dependence of the lattice expansion as compared to the theoretical curve calculated with eqs 1 and 2. Moreover, the data points extend to fluences more than twice higher than F_0^{PLAL}. These observations can be attributed to a much broader size distribution of the PLAL NPs as compared to the CTAB ones (see mass-weighted size distributions in Figure S1c,d in the Supporting Information). Both the NP absorption cross section and the total heat capacity are size dependent, with the former further affected by the NP shapes and agglomeration. As a result, for a given fluence (above or below F_0^{PLAL}), some of the PLAL NPs may be completely molten by the time the probe pulse arrives (60 ps after the pump pulse), while other NPs may only be heated to a temperature significantly below T_m. The melted NPs do not contribute to the crystalline peaks in the diffraction profile, and the shift of the (111) peak reflects the collective contribution of the crystalline NPs heated to different temperatures. As a result, the apparent values of lattice expansion, evaluated for PLAL NPs from the effective shift of the (111) diffraction peak, are lower than those measured for CTAB NPs at all fluences.

The fluence dependence of the (111) peak intensity shown in Figure 1f shows the extent of the loss of crystallinity of the initially monocrystalline CTAB and polycrystalline PLAL NPs by the time of 60 ps after the laser pulse, as well as the recovery of the crystallinity by 1 μs. Both Au NP types undergo a comparable loss of crystallinity with increasing laser fluence by 60 ps, with weak crystalline peaks still detected at fluences as high as 2F_0. The latter observation can be attributed to the NP size polydispersity (Figure S1), with an additional smaller contribution from the 20% local fluence variation across the probed sample volume (see Methods).

The recovery of the intensity of the (111) peak at a delay of 1 μs suggests that the NP cooling due to the heat transfer to the water environment and crystallization of the transiently melted NPs are completed by this time. More importantly, the complete recovery of the crystalline peak intensity observed for PLAL NPs indicate the absence of any significant NP size reduction in the range of fluences covered in Figure 1e,f ($F \leq 2.5F_0$). This conjecture is consistent with the analysis of the fragmentation regimes based on the results of atomistic simulations and SAXS data presented below. At the same time, a substantial reduction the (111) peak intensity observed in Figure 1f for CTAB NPs at a fluence above 2F_0 is indicative of the transformation of the initial single crystal NPs to polycrystalline ones. This transformation is indeed predicted in the atomistic simulations[33] and attributed to the highly

https://doi.org/10.1021/acsnano.3c12314
ACS Nano 2024, 18, 10527−10541

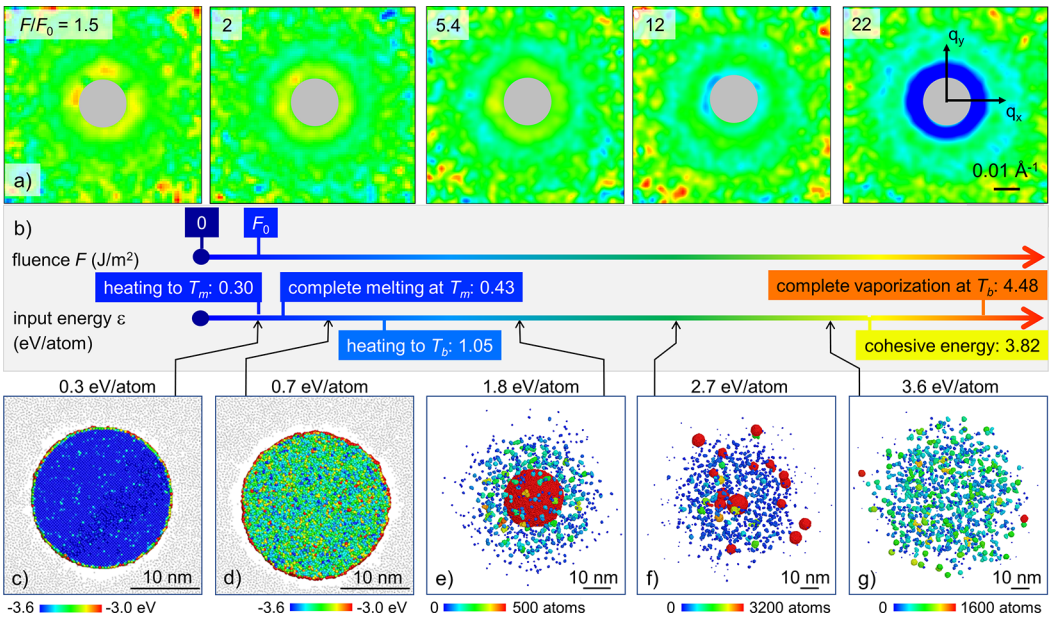

Figure 2. Top panels (a): Selected 2D SAXS difference patterns $\Delta S(q) \times q^2$ measured for CTAB NPs at a delay of 1 μs and shown as false color plots for several fluence values normalized by the threshold fluence F_0^{CTAB}. The color code in the images depict the $\Delta S(q) \times q^2$ patterns at a qualitative level, with blue, green, and red colors corresponding to negative, zero, and positive values. The quantitative information on the relative values of $\Delta S(q) \times q^2$ can be found in Figure 3. The gray areas in the centers of the scattering patterns contain no data, as a beam stop prevents the probe beam from entering the detector. Middle panel (b): The lower arrow shows the reference levels of energy density (eV/atom) required for equilibrium heating, melting, and vaporization of bulk Au material at 1 atm pressure, as well as the cohesive energy of Au. The upper arrow shows a comparable scale of the incident laser fluence, with the threshold fluence for reaching the melting temperature, F_0, used as a reference value for aligning the fluence and energy scales. Bottom panels: Snapshots of atomic configurations obtained in simulations of 20 nm Au NPs irradiated by 10 ps laser pulses at deposited energy densities of 0.3 eV/atom (c), 0.7 eV/atom (d), 1.8 eV/atom (e), 2.7 eV/atom (f), and 3.6 eV/atom (g). The values of energy density deposited by the laser pulse in the simulations are marked in the energy scale by arrows originating from the corresponding snapshots. The atoms in the snapshots are colored by potential energy in (c, d) and by the size (number of atoms) of atomic clusters and NPs they belong to in (e−g). Cross sectional views of halves of the NPs are shown in (c,d), while all Au atoms are shown in (e−g). The CG water particles located within 2 nm-thick slices cut from the central parts of the systems are shown by gray dots in (c, d). The water particles are blanked (not shown) in (e−g) to provide a clear view of the fragmentation products. The snapshots are shown for the times for which the SAXS profiles shown in Figure 3b are calculated, 400 ps in (c, d), 4080 ps in (e), 9040 ps in (f), and 13920 ps in (g).

nonequilibrium nature of the solidification process occurring under conditions of deep undercooling of the molten NPs.

NP Fragmentation Regimes from SAXS Profiles and Atomistic Simulations. While the regime of laser-induced heating, melting, and resolidification is discussed above based on the WAXS data, the transition to the regime of fragmentation can be probed by SAXS measurements, which produce a Fourier transform of the projected scattering length density. Consequently, the SAXS patterns, such as the ones shown in Figure 2a, provide direct access to the laser-induced transformation of the density distributions from compact close-to-spherical NPs to fuzzy clouds of the fragmentation products. The SAXS data in Figure 2a are shown for a delay of 1 μs in the form of 2D difference scattering patterns $\Delta S(\boldsymbol{q}) \times q^2$. A delay of 1 μs is chosen to ensure that most of the rapid dynamic processes (e.g., generation and collapse of cavitation bubbles, or ripening of the fragments[36]) have already decayed. The difference $\Delta S(\boldsymbol{q})$ between the initial scattering distribution (before laser irradiation) and the scattering distribution after laser excitation highlights the general changes in density distributions, such as the disintegration of the initial NPs. Changes to smaller structural features appear at higher scattering vectors and become more visible when $\Delta S(\boldsymbol{q})$ is scaled by q^2, following the Kratky representation.[80]

At laser fluences below $\sim 5F_0$ and a delay of 1 μs, the SAXS data in Figure 2a show the appearance of a relatively weak ring-like pattern featuring a yellow/red ring of increased difference scattering intensity at smallest resolved q values and a weaker light blue ring marking a decreased scattering signal at higher q values. This ring-like pattern can be attributed to a shape transformation from the initially faceted CTAB NPs (see Figure 1a) to spherical NPs of the same volume upon melting. This conjecture is supported by modeling of the $\Delta S(\boldsymbol{q}) \times q^2$ signal due to the NP shape change discussed in Section SI-3 of the Supporting Information and illustrated in Figure S5a,b. The estimation of the fluence threshold F_0 for heating the NPs to T_m is also consistent with the attribution of the ring-like pattern to the melting-assisted NP shape change at fluences above F_0. The evaporation of Au atoms from the surfaces of the irradiated NPs and condensation of these atoms into small satellite NPs may be an additional aspect to consider at fluences above $\sim 3F_0$, although the total amount of material converted to small NPs in this regime ($\varepsilon \leq 6\varepsilon_0$) remains below 20% according to atomistic simulations discussed below.

As the fluence increases above $5F_0$, a pronounced negative (blue) ring appears in the $\Delta S(\boldsymbol{q}) \times q^2$ patterns at small q, signifying the onset of the fragmentation. The fragmentation results in the disappearance of the initial spherical NPs that produce a characteristic scattering pattern $S(\boldsymbol{q})$ featuring a high scattering intensity at low q and a power-law $S(q) \sim q^{-4}$ decline modulated by periodic oscillations, as can be seen in Figure S3a in the Supporting Information.[81] The first

https://doi.org/10.1021/acsnano.3c12314
ACS Nano 2024, 18, 10527−10541

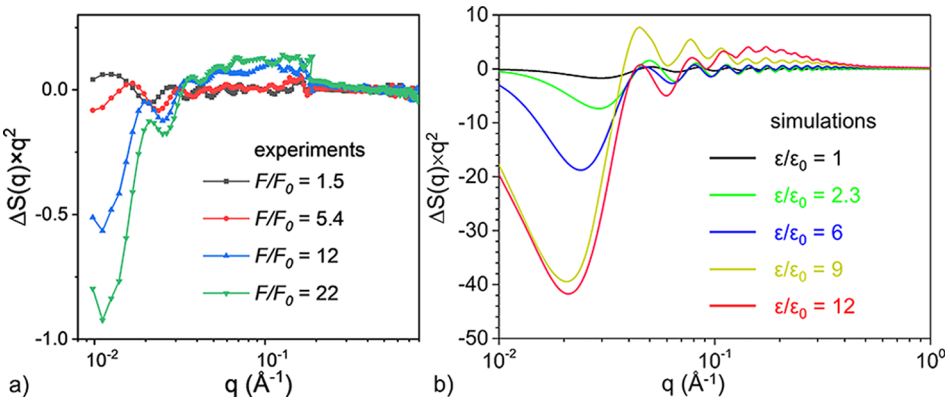

Figure 3. SAXS difference profiles (a) measured in LFL experiments at a delay of 1 μs for 44 nm CTAB NPs and (b) calculated for atomic configurations obtained in simulations of LFL of 20 nm Au NPs and shown in Figure 2c–g. The difference scattering profiles are scaled by q^2 to visualize smaller changes at higher values of q.

minimum of $S(q)$ is located at $q \approx 0.02$ Å^{-1} for the 44 nm CTAB NPs, which causes the negative difference values at $q <$ 0.02 Å^{-1}, and corresponding oscillatory changes at $q >$ 0.02 Å^{-1}. The formation of fragmentation products (small NPs and atomic clusters), on the other hand, is the source of the elevated difference scattering intensity at higher values of q.

Before bringing the analysis of the SAXS data to a more quantitative level, it is instructive to compare the qualitative physical picture suggested by the experiments to the predictions of atomistic simulations of laser interactions with Au NPs in water.[32,33] The snapshots of atomic configurations obtained at the end of the simulations performed at different values of the deposited laser energy density ε are shown in Figure 2c–g. The snapshots are connected by arrows to the energy scale shown in Figure 2b, where the reference levels of energy deposition required for causing the following transformations starting from Au at 300 K are marked:

- heating Au to T_m, ε_0 = 0.3 eV/atom;
- complete melting of Au at T_m, $\varepsilon = 1.43\varepsilon_0$ = 0.43 eV/atom;
- heating Au to the boiling temperature of T_b = 3131 K, $\varepsilon = 3.5\varepsilon_0$ = 1.05 eV/atom;
- completely vaporizing Au at T_b, $\varepsilon = 14.9\varepsilon_0$ = 4.48 eV/atom.

As discussed above, the scales of the incident fluence F and deposited energy ε can be aligned at the thresholds for reaching the melting temperature, F_0 and ε_0, respectively. This alignment of scales is not a trivial issue. In experiments, the incident laser fluence F is known, while the amount of absorbed energy ε could only be approximated. As discussed above, using an example of 44 nm CTAB Au NPs in water, the effective absorption cross section evaluated from the fluence dependence of the lattice expansion deviates from the theoretical value predicted by the Mie theory by more than 50%. Similar discrepancies between the theoretical Mie spectra and the NP absorption evaluated in pump–probe experiments have been reported in earlier studies.[68]

Given this uncertainty, the establishment of quantitative links between experiment and theory is hindered, yet using the reference values of F_0 and ε_0 makes it possible to circumvent the lack of exact knowledge of the absorption cross sections and to align the fluence/energy scales used in the experiments and simulations. The WAXS measurements for CTAB NPs suggest that the scaling of the absorbed laser energy ε with fluence F remains roughly linear, at least up to the melting threshold (Figure 1e). The extension of the assumption of linear scaling of ε with F to higher fluences, however, is questionable, and matching of the reduced fluence and energy scales, F/F_0 and $\varepsilon/\varepsilon_0$, in Figure 2b can be done at a semiquantitative level only. Nevertheless, a series of additional anchor points can be provided at higher fluences by relating the changes in the SAXS profiles observed in the experiments (Figure 2a) to the atomistic picture of the laser-induced structural and phase transformation predicted in the simulations (Figure 2c–g). In particular,

- the complete melting of a NP at $\varepsilon/\varepsilon_0$ = 2.3 (Figure 2d) can be related to the emergence of a weak ring-like pattern attributed in the discussion above to the melting-assisted shape change at $F/F_0 \leq 5$ (e.g., at F/F_0 = 1.5 and F/F_0 = 2 in Figure 2a);
- the evaporation from the surface of a NP and condensation of the metal vapor into atomic clusters and small satellite NPs at $\varepsilon/\varepsilon_0$ = 6 (Figure 2e) may be associated with the onset of the size reduction of the initial NPs, as seen through the decay of $\Delta S(q) \times q^2$ at $q \leq 0.02$ Å^{-1} (e.g., F/F_0 = 12 in Figure 2a);
- the "mild" phase explosion of a NP superheated by the laser energy deposition, where some of the large fragments reflect from the boundary of a transiently forming nanobubble and coalesce into a central large fragment surrounded by smaller fragmentation products at $\varepsilon/\varepsilon_0$ = 9 (Figure 2f),[33] is expected to produce a substantial deepening of the negative ring in the $\Delta S(q) \times q^2$ pattern at small q;
- the "strong" phase explosion leading to the complete disappearance of the initial NP and the formation of a cloud of atomic clusters and small NPs at $\varepsilon/\varepsilon_0$ = 12 (Figure 2g)[32] can be associated with the negative ring at small q reaching its maximum depth (e.g., at F/F_0 = 22 in Figure 2a) as well as the appearance of a positive signal at large q produced by the small NP fragments.

To put the comparison of the computational results and experiments at the quantitative level, the experimental SAXS patterns shown in Figure 2a are radially averaged to produce one-dimensional SAXS difference profiles $\Delta S(q) \times q^2$. The corresponding profiles are also calculated for the atomic configurations predicted in the simulations and shown in Figure 2c–g. The experimental and computational $\Delta S(q) \times q^2$

https://doi.org/10.1021/acsnano.3c12314
ACS Nano 2024, 18, 10527–10541

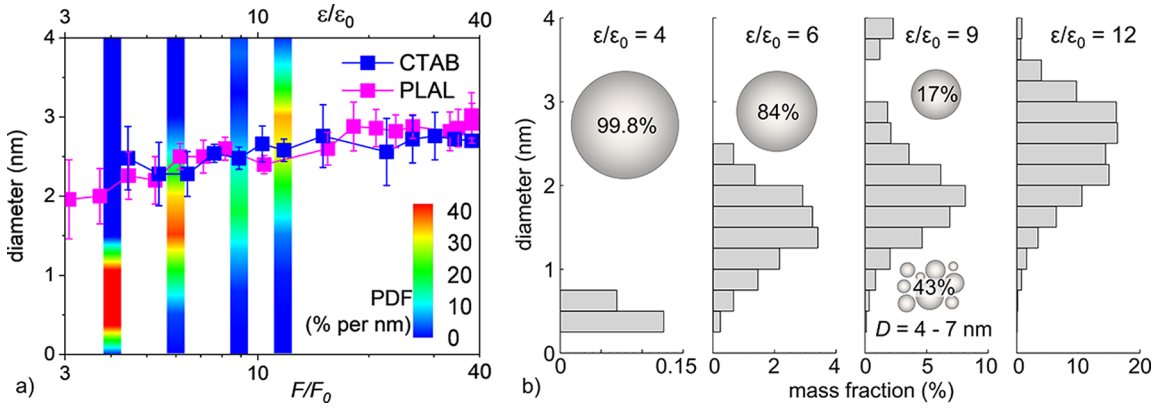

Figure 4. (a) Comparison of the mass-weighted size distributions predicted in the simulations with the characteristic sizes of small NPs obtained by fitting the experimental SAXS profiles, such as the ones shown in Figures 3a and S7, to a simplified model that represents the size distributions by two distinct sizes only. The *x*-axes used for plotting the computational and experimental data are the reduced energy per atom $\varepsilon/\varepsilon_0$ and reduced incident fluence F/F_0, respectively. The distributions shown by color bars in (a) are probability density functions (PDF) defined so that the integral over diameter of all fragments yields 100% (the total mass of the fragmentation products expressed in percent). The atoms in the remaining core NPs present in the simulations performed at $\varepsilon/\varepsilon_0$ = 4, 6, and 9 are not included in the calculation of PDF. The corresponding distributions in (b) are normalized to the total mass of Au in the initial NP, including the remaining core NPs. Note that in the distribution shown in (b) for $\varepsilon/\varepsilon_0$ = 9, large fragments with sizes from 4 to 11 nm are outside the sizerange shown in the figure but account for 60% of the total mass.

profiles, plotted in Figure 3 for comparable ranges of F/F_0 and $\varepsilon/\varepsilon_0$, show similar dependences on the level of laser excitation.

The most striking feature common to the experimental and computational results is the appearance of prominent negative peaks (dips) in the small q regions of the profiles as the level of the laser excitation increases. As briefly discussed above, the appearance of these dips is a signature of the fragmentation of the initial NPs. Assuming a spherical shape of the initial NPs, the scattering profile $S(q)$ can be described by the analytical solution for a spherical particle characterized by a periodically modulated decay of the scattering intensity from its maximum value at q = 0. Using the exponential approximation of the decay of $S(q)$ at small q,[81]

$$S(q) \approx S(0)\exp\left(-\frac{1}{5}q^2R^2\right), \tag{3}$$

we can estimate the position of the first strong peak of $S(q) \times q^2$ produced by an initial spherical NP of radius R as $\sqrt{5}/R$. For CTAB NPs with R = 22 nm and for simulated NPs with R = 10 nm, the peak positions are predicted to be at 0.010 Å^{-1} and 0.022 Å^{-1}, respectively. The fragmentation (i.e., disappearance) of the initial NPs turns the peaks of $S(q) \times q^2$ they produced into the dips of the difference scattering profiles $\Delta S(q) \times q^2$, as illustrated in Figure S3 of the Supporting Information. The positions of these dips in the profiles predicted in the simulations performed at $\varepsilon/\varepsilon_0$ of 9 and 12 (i.e., in the regime of phase explosion)[32,33] are at 0.021 Å^{-1} (Figure 3b), which is within 5% of the value predicted based on the approximate eq 3. This deviation from the theoretical value can be largely attributed to the approximate nature of eq 3, which becomes less accurate as q increases above $1/R$.[81] The deviation of the position of the dip in the experimental profile at F/F_0 = 22, 0.012 Å^{-1}, from the theoretical value estimated for a spherical 44 nm NP is somewhat larger, which may be related to the recognizable nonuniformaties of the shape (from spheres) and size distribution (see Section SI-1 in the Supporting Information).

Another notable characteristic of the experimental and computational $\Delta S(q) \times q^2$ profiles is the appearance of positive features in the higher q range, at q > 0.1 Å^{-1}, in all the experiments and simulations where the negative dip is observed at lower values of q. Consequently, these positive features in the difference scattering profiles can be directly linked to the fragmentation and attributed to the generation of atomic clusters and small NPs, such as the ones present in the snapshots shown in Figure 2f,g. Indeed, the increase in F/F_0 or $\varepsilon/\varepsilon_0$ above the fragmentation threshold results in the growth of the positive features of $\Delta S(q) \times q^2$ and their shift to a higher q region. These changes can be attributed to smaller sizes of the fragmentation products, as evident from the comparison of snapshots shown in Figure 2f,g.

One noteworthy difference between the experimental and computational $\Delta S(q) \times q^2$ profiles is seen in the low q range at low laser fluences (F/F_0 of 1.5 and 5.4 and low deposited laser energies ($\varepsilon/\varepsilon_0$ of 1.0 or 2.3), i.e., below the fragmentation threshold. The experimental $\Delta S(q) \times q^2$ profiles obtained for CTAB NPs exhibit a slight increase followed by oscillations at low values of q, while the simulated profiles have dips in the same range of q. In the simulation performed at $\varepsilon/\varepsilon_0$ = 1.0, the $\Delta S(q) \times q^2$ profile exhibits only a weak decrease that can be attributed to the thermal expansion of the NP, which has not been melted and has cooled down to $0.71T_m$ by the time of 400 ps, when the scattering profile is calculated. At $\varepsilon/\varepsilon_0$ = 2.3, the dip at low q is more pronounced, which can be attributed to an additional increase in the NP size upon melting. At this energy density, the maximum temperature of the NP reaches $1.46T_m$, and the NP cools down to $1.35T_m$ by 400 ps, when the scattering profile is calculated. No evaporation is observed at this energy density, and the NP is expected to cool down and solidify within several nanoseconds. Indeed, the NP in this simulation is observed to cool down to $0.95T_m$ by the end of the simulation at 2 ns, although it still remains in the (supercooled) molten state at this time. The thermal expansion and melting, therefore, are not expected to contribute to the experimental scattering profiles measured at a delay of 1 μs. The increase in the SAXS difference profiles at low q observed in Figure 3a at low fluences can be explained by the transformation of faceted CTAB NPs (Figure 1a) to spheres

https://doi.org/10.1021/acsnano.3c12314
ACS Nano 2024, 18, 10527−10541

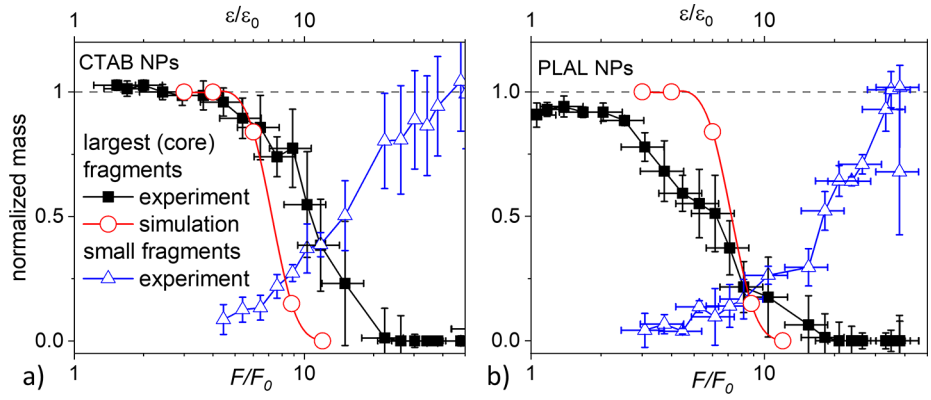

Figure 5. Fluence dependences of the mass fractions of the largest fragments (black squares) and small NPs (blue triangles) obtained from the fits of the SAXS data measured for CTAB (a) and PLAL (b) NPs. The red circles show the mass fraction of the largest fragments predicted in the atomistic simulations for different values of the deposited energy density (upper *x*-axis). The mass of small fragments has been multiplied by 1.2 for CTAB and 0.7 for PLAL, with an explanation of this scaling provided in Section SI-3 of the Supporting Information.

upon complete or partial melting of the NPs. The corresponding changes in the $\Delta S(q) \times q^2$ profile are not observed in the simulations or in experiments performed for PLAL NPs (see Section SI-5 in the Supporting Information), where the initial NPs are spherical. The increase in the SAXS difference signal at low q can also be reproduced by the fitting procedure assuming that 1−2% of the particles have fused into larger ones, an effect that is related to the size shaping in so-called laser melting in liquid (LML).[35,82]

Fitting the SAXS Data to a Simplified Model. Apart from the comparison of the differential scattering patterns measured in experiments and predicted in the atomistic simulations, it is instructive to compare the sizes of fragmentation products generated at similar levels of reduced fluence and energy (F/F_0 and $\varepsilon/\varepsilon_0$, respectively). To obtain the information on the characteristic sizes of NP fragments from the $\Delta S(q) \times q^2$ profiles, the experimental scattering profiles are fitted to a simplified analytical model that considers a combined effect of the shape transformation (for CTAB NPs only, due to their faceted shapes) and the fragmentation of the initial NPs into large core NPs and a population of small fragments represented by a single size value. In this fitting model, the complexity of the real size distributions is reduced to two characteristic sizes, those of the remaining core NPs and the smaller fragments. The details of this analytical model and the fitting procedure are provided in Section SI-3 of the Supporting Information. The results of the fitting are displayed together with the experimental data in Figure S7 and Table S1 in Section SI-5 of the Supporting Information.

Note that for the PLAL NPs a sufficient agreement between the SAXS-fitting model and the experimental data was only achieved by considering an additional contribution with an effective length scale D_a (or $2R_a$ in Figure S4 of the Supporting Information). This additional contribution represents a "secondary structure" in the mass distribution and can be understood as a positional correlation (e.g., agglomeration or spacing) among the small NP fragments. A comparison between the result obtained for PLAL and CTAB NPs shows that the positional correlation is much weaker for CTAB NPs, where the abundance of CTAB surfactant (3 mM versus 0.5 mM gold atoms) stabilizes the small fragments against agglomeration. Since the positional correlation with the length scale D_a does not make its own separate contribution to the total mass of the fragmentation products, it is not considered further when comparing the size and mass balance of the fragments in Figures 4 and 5, respectively.

The sizes of the small NPs produced by the fitting procedure applied to the SAXS profiles measured at different fluences are plotted in Figure 4a. The fluence dependence is characterized by a slight growth in size from 2.0 to 2.9 nm for both PLAL and CTAB NPs. The increase of the gained particle size with F/F_0 is similar in experiments performed for PLAL and CTAB NPs, despite the significantly broader initial particle size distribution of the PLAL NPs. From a synthesis point of view, this similarity indicates that the diameter of the nanoparticles gained from laser fragmentation in liquids is rather insensitive to the initial particle size distribution, which is beneficial for the reproducibility of the laser fragmentation and encouraging for scaling and implementation of the laser fragmentation in the context of a scaled nanoparticle synthesis on g- or even kg-scale.[83,84]

The general trend of the increasing size of the fragmentation products with increasing fluence is also observed in the size distributions predicted in the atomistic simulations, which are shown in the form of color bars in Figure 4a and histograms in Figure 4b. The size increase in the simulations, however, is more pronounced. The size distribution of the fragmentation products changes from atomic clusters with sizes below 1 nm at $\varepsilon/\varepsilon_0$ = 4 and NPs smaller than 2.5 nm at $\varepsilon/\varepsilon_0$ = 6, in the regime of evaporation and condensation, to a trimodal distribution characterized by three distinct peaks at 1−3 nm (40% mass fraction), 4−7 nm (43% mass fraction), and an 11 nm NP (17% mass fraction) at $\varepsilon/\varepsilon_0$ = 9, in the regime of "mild" phase explosion. Upon further increase of the deposited energy, the fragmentation goes into the regime of "strong" phase explosion, where the size distribution shrinks to a unimodal one. This transition is exemplified by a distribution observed at $\varepsilon/\varepsilon_0$ = 12, where all fragments are smaller than 4 nm.

While the representation of all small fragmentation products by a single size in the fitting model cannot capture the complex fluence dependence of the size distributions predicted in the atomistic simulations, the overall trend of increasing size of the small fragments is still captured by the simplified fitting model. The experimentally and computationally obtained sizes agree particularly well in the intense evaporation and mild phase

https://doi.org/10.1021/acsnano.3c12314
ACS Nano 2024, 18, 10527−10541

explosion regimes, where F/F_0 and $\varepsilon/\varepsilon_0$ range from 6 to 10. At lower fluences, where F/F_0 and $\varepsilon/\varepsilon_0$ are below 6, the sizes determined from the SAXS data (~2 nm) exceed the sizes of atomic clusters observed in the simulation (<1 nm at $\varepsilon/\varepsilon_0 = 4$, Figure 4b). In this context, we note that the sensitivity of SAXS toward smaller particles drops quickly, so that the clusters below 1 nm may simply not have been detected. The much longer probe delay time of 1 μs, as compared to the nanosecond time scale of the simulations, may also be a factor contributing to the growth of the atomic clusters into small nanoparticles.

The broadening of the size distributions at higher fluences, in the regime of strong phase explosion (e.g., $\varepsilon/\varepsilon_0 = 12$ in Figure 4b), presents another challenge to the simplified fitting model. While a more complex size distribution with up to 3 individual size fractions could have been included in the SAXS data analysis, the larger number of parameters would also require sufficient boundary conditions/constraints as well as longer data acquisition to further reduce the noise. The design of a more sophisticated SAXS fitting model will be the next step, whereby the atomistic simulations will provide the needed constraints and model verification.

The transition between the fragmentation regimes is more apparent from the plots of the mass fractions of the "large" and "small" fragments yielded by the SAXS fitting procedure and plotted in Figure 5. The mass fraction of the large fragments, which usually correspond to the parts of the initial NPs that survive the fragmentation process, undergoes a change from 100 to 0% in a range of F/F_0 from 3 to 20 for CTAB NPs, Figure 5a. The corresponding transition of the mass fraction of the largest fragment predicted in the atomistic simulations takes place in a narrower range of absorbed energy $\varepsilon/\varepsilon_0$, from 5 to 10, and is attributed to the transition to the phase explosion regime of LFL. The wider transition region in the experiments can be explained by the polydispersity of the NPs and the 20% variation of the local fluence across the probed sample volume (see Methods). Indeed, the much broader size distribution of PLAL NPs (Figure S1 in the Supporting Information) results in a weaker decline of the mass fraction of the large fragments with increasing fluence, Figure 5b. For both CTAB and PLAL NPs, the reduction of the size of the largest fragments is accompanied by an appearance of small fragments, where the masses of the large and small NPs roughly balance.

CONCLUSION

The results of a well-integrated computational and experimental study of picosecond laser fragmentation of Au NPs in water has revealed a sequence of distinct fluence regimes of laser-NP interactions. At low laser fluences, below the threshold for NP melting, the laser-induced processes are limited to the NP heating by the laser excitation and cooling due to the heat transfer to the surrounding water. The lattice expansion, measured from the shift of the (111) Bragg peak position at a time delay of 60 ps, yields information on the maximum NP lattice temperature reached by the time when the excited electrons have equilibrated with the lattice, but the heat dissipation into the water environment is still negligible. For CTAB NPs featuring a narrow size distribution, the expansion of NPs is found to be well described by a curve obtained with the temperature-dependent coefficient of thermal expansion and heat capacity of bulk gold, assuming a constant (fluence-independent) value of the NP absorption cross section. The latter is not generally expected and is explained by the transient variation of the absorption cross section during the laser pulse, as the optical properties of the NPs get in and out of the plasmon resonance under the 400 nm laser irradiation. The lattice expansion that corresponds to the melting temperature of CTAB NPs is subsequently used to define the fluence threshold F_0 for reaching the melting temperature and to match it with the corresponding theoretical energy density ε_0, thus aligning the fluence and energy scales used in the experiments and atomistic modeling, respectively.

Despite the absence of any significant NP size reduction in the regime of melting and resolidification, a substantial reduction the (111) peak intensity is observed for CTAB NPs at a time delay of 1 μs, i.e., after solidification of the transiently melted NPs. The results of atomistic simulations suggest that the reduction of the Bragg peak intensity may be related to the transformation of the initial single crystal NPs to polycrystalline NPs featuring a high density of crystal defects generated in the course of rapid solidification proceeding under conditions of deep undercooling below T_m. Another implication of the transient melting process is the transformation of the initially faceted CTAB NPs to spherical shapes, as evidenced by the corresponding SAXS difference profiles measured at fluences exceeding F_0.

The regime of melting and resolidification extends up to about $3F_0$ (or $3\varepsilon_0$ in the simulations). Above this fluence/energy density level, the appearance of first atomic clusters and small NPs is observed in the atomistic simulations and is deduced from analysis of the SAXS profiles. The formation of small (below 2.5 nm, according to the simulations) NPs is attributed to the transition to the regime of evaporation of Au atoms from the surfaces of irradiated NPs and condensation of the metal vapor into small NPs surrounding the remaining core NP. The formation of small fragments in this irradiation regime occurs on the nanosecond time scale, during the lifetime of nanobubbles forming around the irradiated NPs, and produces a core−satellite arrangement of the fragmentation products. The central core NPs in this regime make the dominant contribution to the mass-weighted size distribution of the fragmentation products.

Further increase of the laser fluence in experiments above $5F_0$ and the deposited energy density in simulations above $6\varepsilon_0$ results in the transition from the evaporation−condensation regime of LFL to the regime of so-called "phase explosion," i.e., a rapid (explosive) phase decomposition of the superheated Au NPs into small liquid droplets and vapor-phase atoms. The simulations reveal two distinct regimes of the phase explosion: (1) a "mild" phase explosion[33] characterized by a broad distribution of the fragmentation products, with some of the large fragments reflecting from the boundary of transiently forming nanobubbles due to the inverse Leidenfrost effect and coalescing into large central fragments surrounded by smaller fragmentation products, and (2) a "strong" phase explosion[32] proceeding through a prompt disintegration of the NPs into vapor, atomic clusters, and NPs with sizes that do not exceed several nanometers.

The transition to the phase explosion regime of LFL is signified by prominent changes in the SAXS difference profiles $\Delta S(q) \times q^2$ measured in experiments and calculated for atomic configurations produced in the simulations. First, there is an appearance of negative peaks (dips) in the small q regions of the scattering difference profiles. These dips are unambiguously attributed to the disappearance (fragmentation) of the initial NPs by quantitative analysis of the dip positions in the

https://doi.org/10.1021/acsnano.3c12314
ACS Nano 2024, 18, 10527−10541

experimental and simulated $\Delta S(q) \times q^2$ profiles. Second, the emergence of the elevated difference scattering intensity in the higher q range, at $q > 0.1$ Å^{-1}, is observed in all experiments and simulations performed in the phase explosion irradiation regime. The positive features in the difference scattering profiles become more pronounced and shift to higher values of q with increasing fluence/energy density, which can be directly linked to changes in the fragmentation product size distribution upon the transition from the "mild" to the "strong" phase explosion regime of LFL.

The very good agreement in the dependences of the experimental and computational SAXS profiles on the level of laser excitation, observed for comparable ranges of F/F_0 and $\varepsilon/\varepsilon_0$, provides strong support for the mechanistic picture of the sequence of distinct regimes of laser−colloidal NP interactions. As the laser fluence increases, these regimes shift from heating and cooling, to melting and resolidification, to evaporation and condensation leading to the formation of core−satellite arrangement of the fragmentation products, and finally to the "mild" and "strong" phase explosion leading to the complete disintegration of the initial NPs. This agreement encourages an extension of the joint computational and experimental efforts to probe the time-resolved dynamics of the fragmentation process, including the evolution of the nanobubble, kinetics of the formation, coarsening, and solidification of the fragmentation products. The improved understanding of the mechanisms of laser processing and fragmentation of colloidal NPs will, in turn, enable tuning of the sizes, shapes, and internal structures of NPs to the needs of practical applications.

METHODS

Experimental Setup and Data Analysis. The pump-probe experiment is conducted with a picosecond laser (pulse duration of 1 ps) used as an excitation (pump) source while the pulsed emission from the European Synchrotron Radiation Facility (ESRF) storage ring at the beamline ID09 was used as the time-resolved X-ray probe (pulse duration of 60 ps), both at a repetition rate of 1 kHz. The pump and the probe beams are focused on a free circular jet of a colloidal solution of mono- and polycrystalline gold NPs gained from chemical synthesis (labeled CTAB after the main surfactant) and PLAL, respectively. The wavelength of the pump pulse, 400 nm, is chosen to match the interband excitation of the NPs, so that efficiency losses due to intrapulse bleaching at the plasmon resonance are minimized.[68,85,86] The experimental setup is schematically illustrated in Figure 1c and described in detail in earlier publications.[36,68] A few key points are briefly outlined below.

Colloid Synthesis. Two types of NPs are used in the experiments. The first type of NPs is chemically prepared colloids with mostly single-crystalline NPs featuring faceted shapes obtained from a seeded growth with cetyltrimethylammonium bromide (CTAB, ACROS chemicals) as a surfactant.[57] A representative TEM image is shown in Figure 1a together with the particle size distributions in Figure S1a,c and high resolution image in Figure S2a. Given single-crystallinity and monodispersity of the gold colloids, the chemically prepared gold nanoparticles represent our model system in this study. The second type is NPs prepared by batch ablation of a gold target in Milli-Q water using a focused pulsed Nd:YAG laser (Ekspla, Atlantic Series, 10 ps, 1064 nm, 9.6 mJ, 100 kHz, 10 min in 30 mL batches), similar to previous studies.[24,36,58] The larger (40−70 nm) gold particles are collected and separated from smaller fractions by a two-step fractional centrifugation (Hettich, Universal 320, 1000 kRPM, 95G in 50 mL Falcon tubes). In the first step the particle fraction >40 nm is retrieved as a pellet, separated from the supernatant, and redispersed in a NaOH/NaCl solution. This protocol was repeated one more time to remove residual small size fractions. As shown in Figure S1b, the final colloid still contained some smaller (<10 nm) nanoparticles whose mass (SAXS is volume-sensitive) was however neglectable, as shown by the mass-weighted particle size distribution in Figure S1d. Both the representative TEM image in Figure 1a and the high-resolution image in Figure 2b of the Supporting Information show that mostly spherical Au NPs were gained by the laser synthesis. Given previous theoretical predictions,[15,17,87] the spherical NPs from laser ablation in liquids are likely to be enriched with internal planar defects. Consequently, the laser-generated nanoparticles, despite their polydispersity, were included to determine how sensitive our study concept (joining theory and experiment) and the synthesis procedure (LFL) are to the initial particle size distribution, which is characteristic for the laser synthesis. From the experimental SAXS profiles determined during the pump−probe experiments, the best fitting (methodology: see subsection Scattering Data Analysis below) for the initial Au NPs was obtained with NP diameter $(2R_i)_{SAXS}$ of 44 and 50 nm for CTAB and PLAL particles, respectively. These particle sizes are in good agreement with the TEM images shown in Figure 1a,b and Figure S2, as well as the corresponding size distributions provided in Figure S1 of the Supporting Information.

Laser Excitation and X-ray Probing of the Laser-induced Fragmentation Process. During the *in situ* (laser-)pump-(X-ray-)probe fragmentation experiment, a pulsed X-ray beam (Synchrotron, ID09, ESRF facility, pulse duration of 60 ps) with a diameter of only 40 μm is directed onto the central section of the cylindrical colloid-liquid jet that had a diameter of 270 μm (see Figure 1c). A ps-laser (Coherent Evolution, frequency-doubled by a BBO crystal, intensity controlled by a combination of waveplate and polarizer) with a Gaussian laser spot size of 0.22 mm full width at half-maximum (FWHM) was directed onto the central part of the liquid jet and overlapped centrally with the X-ray beam. Note that the effect of refraction-induced focusing due to the cylindrical colloid jet[88] is significantly reduced due to the smaller diameter of the X-ray probe compared to the diameters of the jet and the laser pulse. The effects of extinction with depth and astigmatic laser beam propagation with an 8-degree mismatch between both beams are kept at a minimum, but the fluence variation is estimated to be 20% across the probed sample volume.[68] Other parameters, such as focusing or jet diameter, may vary for different experimental runs. Therefore, it is useful to internally scale the fluence as a function of the observed structural response, in particular the onset of melting F_0. Data from two experiments are discussed here, and the corresponding values of F_0 are F_0^{CTAB} = 32 J/m^2 and F_0^{PLAL} = 40 J/m^2 for the data sets plotted in Figure 1 and F_0^{CTAB} = 36 J/m^2 and F_0^{PLAL} = 52 J/m^2 for the data sets plotted in Figures 2−5 and in Supporting Information. The estimated error in F_0 is 10%.

Scattering Data Collection. The scattering from the excited colloid (sketch in Figure 1c) is collected by a 2D detector (Rayonix 170HS) at a fixed temporal delay (in steps as small as 5 ps up to 1 μs). The scattering data are integrated over 5000 and 10000 probe pulses for SAXS and WAXS, respectively. The photoexcitation difference data ΔS are obtained by subtracting scattering signal recorded at a negative delay; i.e., the X-ray pulse arrives prior to the laser pulse. The SAXS at a detector distance of 640 mm covers a range of $q = (4\pi/\lambda)\sin(2\theta/2)$ from 0.009 to 0.27 Å^{-1}, as limited by the smallest scattering angle 2θ and the count rate at large angles. In WAXS, an interval from 0.27 to 5 Å^{-1} is covered. Analysis of the WAXS data is done by extracting the gold powder peaks from the large background of the water liquid scattering[89] and analyzing, in particular, the (111) reflection for peak shift, intensity, and broadening. The resolution of broadening is limited through the finite energy bandwidth of the X-ray beam of about 1%.[90] For the particle shape analysis, the scattering intensities in SAXS and WAXS were combined by using a scale factor that accounts for the exposure time and space angle coverage of the pixels.

Scattering Data Analysis. The observables from WAXS are (a) the peak shift of the (111) powder reflection as an indication of lattice expansion, (b) reduction of the peak intensity due to thermal vibrations (Debye−Waller factor)[91] or particle melting, and (c) peak broadening that could stem from a reduction of particle size or from appearance of internal strain/defects. The signal contribution due to

https://doi.org/10.1021/acsnano.3c12314
ACS Nano 2024, 18, 10527−10541

liquid scattering in general shows signatures of heating and related pressure changes[36] but is not addressed here. The interpretation of the SAXS data is assisted by fitting the difference scattering profile $\Delta S(q)$ to a simplified model assuming a linear combination of the contributions from the following transformations experienced by the irradiated NPs. First, the CTAB NPs undergo a volume-conserving shape transformation from the initially faceted (cuboid) morphology to the spherical shape upon melting. Second, both CTAB and PLAL NPs can undergo fragmentation, yielding a core NP of a smaller radius and a number n_s of small (denoted by subscript s) fragments with radius R_s. The population of final (denoted by subscript f) core NPs is characterized by a Gaussian distribution of radii with a mean value of R_f and a standard deviation of σ_f, as implemented in a Python code from PySAXS.[92] The small fragments are modeled by the generalized approach introduced by Beaucage,[93] using the number of small nanoparticles n_s, their radius R_s and the Porod slope d. This slope is fixed to 4 to avoid an underdetermined set of variables. Finally, the positional correlations of smaller NPs are introduced by an additional spatial parameter $2R_a$, which accounts for the arrangement of small NPs with respect to each other, including the effect of possible agglomeration. The positional correlation is introduced via a second generalized function with weight factor n_a and a Porod slope of 4. A more detailed description of the fitting procedure is provided in Section SI-3 of the Supporting Information.

Atomistic Simulations and Calculation of the SAXS Profiles. The simulations of LFL of a 20 nm Au NP irradiated in water by a 10 ps laser pulse are performed with a hybrid computational model that combines a continuum-level description of the laser excitation of the electronic subsystem of the NP and electron−phonon equilibration, a fully atomistic MD modeling of the structural and phase transformations triggered by the laser excitation, and a coarse-grained (CG) MD representation of the aqueous environment. A detailed description of the model is provided in ref 32. Below we only outline the key aspects of the computational setup and describe the method used for the calculation of the diffraction profiles from the atomic configurations predicted in the simulations.

Computational Setup for Simulation of LFL. The initial colloidal NP is located in the center of a spherical computational domain and is surrounded by liquid. The response of the NP to the laser energy deposition is represented with a fully atomistic model combining classical MD with a continuum description of laser excitation of the conduction band electrons and electron−phonon coupling based on the two-temperature model (TTM).[94,95] The TTM-MD model is adapted for the specifics of laser interaction with colloidal NPs. In particular, the dependence of the effective strength of the electron−phonon coupling on the size of NPs and atomic clusters[69,70,96] is introduced through an on-the-fly cluster analysis identifying sizes of all fragmentation products in the course of the simulation.[32] The laser excitation of the electrons in the NP is represented through a source term added to the TTM equation for the electron temperature.[94]

The interactions between Au atoms are described by the embedded atom method (EAM) potential[97] that provides an accurate description of the experimental properties of Au, including the melting temperature of T_m = 1330 K, enthalpy of melting of H_m = 0.13 eV/atom, and cohesive energy of E_c = 3.81 eV/atom. The corresponding experimental values[71] are T_m = 1337 K, H_m = 0.13 eV/atom, and E_c = 3.82 eV/atom. The liquid surrounding the NPs is represented by a CG MD model,[98,99] where an internal heat bath approach is used to ensure that the experimental heat capacity of water is reproduced. The thickness of the liquid shell represented with the CG MD model is 50 nm, which is sufficient to ensure that all the fragmentation products remain within the computational domain during the simulation. In total, the MD equations of motion are solved for more than 240 000 Au atoms and more than 1.1×10^7 CG particles. The reflection-free propagation of the laser-induced spherical pressure wave from the computational domain to the surrounding water environment is represented by the acoustic impedance matching boundary condition[100,101] applied to the outer boundary of the CG liquid shell, which changes its radius during the simulation.

Calculation of the Diffraction Profiles. In order to directly relate the results of the atomistic simulations of LFL to the experimental probing of the fragmentation process, the small and wide-angle scattering profiles are calculated for atomic configurations predicted in the simulations. The spherically averaged powder-diffraction structure factor $S(q)$ measured in the experiments can be calculated with the Debye scattering equation, which, for a monatomic system, takes a form of[102]

$$S(q) = 1 + \frac{2}{N}\sum_{j=1}^{N}\sum_{i>j}^{N}\frac{\sin(qr_{ij})}{qr_{ij}} \tag{4}$$

where $r_{ij} = |\vec{r}_i - \vec{r}_j|$ is the interatomic distance between atoms i and j, N is the total number of atoms, and the summation is over all pairs of atoms in the system. To avoid the computationally expensive summation over all pairs of atoms, the double sum in eq 4 can be substituted by a sum over bins of a histogram $h(r_k)$ containing the number of interatomic distances that fall within the bins with a width of Δr centered at $r_n = k \times \Delta r$. The Debye equation then takes the form analogous to the Fourier transform of the pair density function, $\rho(r) = h(r)/(2\pi r^2 \Delta r N)$:

$$S(q) = 1 + \int_0^\infty 4\pi r^2 \rho(r)\frac{\sin(qr)}{qr}\,dr = 1 + \frac{2}{N}\sum_{k=1}^{N_b} h(r_k)\frac{\sin(qr_k)}{qr_k} \tag{5}$$

where N_b is the total number of histogram bins chosen so that the histogram covers all distances found in the atomic configuration of interest. The bin size used in the calculations reported in this paper is $\Delta r = 10^{-3}$ Å.

ASSOCIATED CONTENT

Supporting Information

The Supporting Information is available free of charge at https://pubs.acs.org/doi/10.1021/acsnano.3c12314.

(1) Figures showing the size distributions and TEM images of Au NPs used in the present study,
(2) an illustration of the manifestation of the NP fragmentation in the scattering profiles shown as $S(q)$, $S(q) \times q^2$, and $\Delta S(q) \times q^2$,
(3) description of the procedure for fitting the SAXS curves with the used formulas,
(4) powder diffraction profiles measured in the experiment and predicted in atomistic simulations,
(5) difference scattering curves for NPs irradiated at different fluences F/F_0 and a table containing the corresponding fitting parameters (PDF)

AUTHOR INFORMATION

Corresponding Author

Sven Reichenberger − *Department of Technical Chemistry I and Center for Nanointegration Duisburg-Essen, University of Duisburg-Essen, D-45141 Essen, Germany;* orcid.org/0000-0002-7166-9428; Email: sven.reichenberger@uni-due.de

Authors

Anton Plech − *Institute for Photon Science and Synchrotron Radiation, Karlsruhe Institute of Technology, D-76344 Eggenstein-Leopoldshafen, Germany;* orcid.org/0000-0002-6290-9303

Meike Tack − *Department of Technical Chemistry I and Center for Nanointegration Duisburg-Essen, University of Duisburg-Essen, D-45141 Essen, Germany*

Hao Huang − *Department of Materials Science and Engineering, University of Virginia, Charlottesville, Virginia*

https://doi.org/10.1021/acsnano.3c12314
ACS Nano 2024, 18, 10527−10541

22904-4745, United States; School of Mechanical Science and Engineering, Huazhong University of Science and Technology, Wuhan 430074, China

Mikhail Arefev − *Department of Materials Science and Engineering, University of Virginia, Charlottesville, Virginia 22904-4745, United States*

Anna R. Ziefuss − *Department of Technical Chemistry I and Center for Nanointegration Duisburg-Essen, University of Duisburg-Essen, D-45141 Essen, Germany*

Matteo Levantino − *European Synchrotron Radiation Facility, F-38043 Grenoble, France;* orcid.org/0000-0002-1224-4809

Hasan Karadas − *Institute for Photon Science and Synchrotron Radiation, Karlsruhe Institute of Technology, D-76344 Eggenstein-Leopoldshafen, Germany*

Chaobo Chen − *Department of Materials Science and Engineering, University of Virginia, Charlottesville, Virginia 22904-4745, United States*

Leonid V. Zhigilei − *Department of Materials Science and Engineering, University of Virginia, Charlottesville, Virginia 22904-4745, United States;* orcid.org/0000-0002-1549-7086

Complete contact information is available at: https://pubs.acs.org/10.1021/acsnano.3c12314

Author Contributions

The research has been designed by A.Z., S.R., L.V.Z., and A.P. The experiments have been performed by A.Z., S.R., M.L., M.T., H.K., and A.P. First analysis has been performed by A.P., and final analysis and comparison to theory were done by all coauthors. The MD simulations and analysis of the computational results have been performed by H.H., M.A., C.C., and L.V.Z. The manuscript has been written by S.R., L.V.Z., and A.P. with input from all authors.

Notes

The authors declare no competing financial interest.

ACKNOWLEDGMENTS

This work is supported by Deutsche Forschungsgemeinschaft under contract PL325/10-1 and RE4672/2-1, by the National Science Foundation (NSF) through grants CMMI-2302577 and CBET-2126785, and by the Helmholtz Association program "From Matter to Materials and Life." L.V.Z. also acknowledges the Research Award from the Alexander von Humboldt Foundation. Computational support was provided by the NSF through the Advanced Cyberinfrastructure Coordination Ecosystem: Services & Support (ACCESS) project DMR110090. The beam time is provided by ESRF (ID9, experiments SC5032 and SC5265) and KIT Light source, with the SAXS apparatus operated in cooperation with group of H. Nirschl. The authors acknowledge technical support at the beamline at KIT Light source by G. Buth (Karlsruhe Institute of Technology) and assistance with HR-TEM analysis by H. Störmer (Karlsruhe Institute of Technology). The institute IBPT at KIT is acknowledged for operation of the accelerator KARA at KIT.

REFERENCES

(1) Torresan, V.; Guadagnini, A.; Badocco, D.; Pastore, P.; Muñoz Medina, G. A.; Fernàndez van Raap, M. B.; Postuma, I.; Bortolussi, S.; Bekić, M.; Čolić, M.; Gerosa, M.; Busato, A.; Marzola, P.; Amendola, V. Biocompatible Iron-Boron Nanoparticles Designed for Neutron Capture Therapy Guided by Magnetic Resonance Imaging. *Adv. Healthc. Mater.* **2021**, *10*, No. 2001632.

(2) Bailly, A.-L.; Correard, F.; Popov, A.; Tselikov, G.; Chaspoul, F.; Appay, R.; Al-Kattan, A.; Kabashin, A. V.; Braguer, D.; Esteve, M.-A. In vivo Valuation of Safety, Biodistribution and Pharmacokinetics of Laser-synthesized Gold Nanoparticles. *Sci. Rep.* **2019**, *9*, No. 12890.

(3) Hupfeld, T.; Salamon, S.; Landers, J.; Sommereyns, A.; Doñate-Buendía, C.; Schmidt, J.; Wende, H.; Schmidt, M.; Barcikowski, S.; Gökce, B. 3D Printing of Magnetic Parts by Laser Powder Bed Fusion of Iron Oxide Nanoparticle Functionalized Polyamide Powders. *J. Mater. Chem. C* **2020**, *8*, 12204−12217.

(4) Doñate-Buendia, C.; Kürnsteiner, P.; Stern, F.; Wilms, M. B.; Streubel, R.; Kusoglu, I. M.; Tenkamp, J.; Bruder, E.; Pirch, N.; Barcikowski, S.; Durst, K.; Schleifenbaum, J. H.; Walther, F.; Gault, B.; Gökce, B. Microstructure Formation and Mechanical Properties of ODS Steels Built by Laser Additive Manufacturing of Nanoparticle Coated Iron-Chromium Powders. *Acta Mater.* **2021**, *206*, No. 116566.

(5) Zhang, D.; Liu, J.; Li, P.; Tian, Z.; Liang, C. Recent Advances in Surfactant-Free, Surface-Charged, and Defect-Rich Catalysts Developed by Laser Ablation and Processing in Liquids. *ChemNanoMater.* **2017**, *3*, 512−533.

(6) Reichenberger, S.; Marzun, G.; Muhler, M.; Barcikowski, S. Perspective of Surfactant-Free Colloidal Nanoparticles in Heterogeneous Catalysis. *ChemCatChem.* **2019**, *11*, 4489−4518.

(7) Forsythe, R. C.; Cox, C. P.; Wilsey, M. K.; Müller, A. M. Pulsed Laser in Liquids Made Nanomaterials for Catalysis. *Chem. Rev.* **2021**, *121*, 7568−7637.

(8) Guo, H.; Tong, Y.; Fan, H.; Ye, Q.; Zhang, J.; Wang, H.; Cao, F.; Li, L.; Wang, H. Embedding Laser-Generated GaAs Nanocrystals in Perovskite Wires for Enhanced Charge Transport and Photodetection. *Sci. China-Phys. Mech. Astron.* **2022**, *65*, No. 274204.

(9) Zhang, D.; Gökce, B.; Barcikowski, S. Laser Synthesis and Processing of Colloids: Fundamentals and Applications. *Chem. Rev.* **2017**, *117*, 3990−4103.

(10) Xiao, J.; Liu, P.; Wang, C. X.; Yang, G. W. External Field-Assisted Laser Ablation in Liquid: An Efficient Strategy for Nanocrystal Synthesis and Nanostructure Assembly. *Prog. Mater. Sci.* **2017**, *87*, 140−220.

(11) Amans, D.; Cai, W.; Barcikowski, S. Status and Demand of Research to Bring Laser Generation of Nanoparticles in Liquids to Maturity. *Appl. Surf. Sci.* **2019**, *488*, 445−454.

(12) Amendola, V.; Amans, D.; Ishikawa, Y.; Koshizaki, N.; Scirè, S.; Compagnini, G.; Reichenberger, S.; Barcikowski, S. Room-Temperature Laser Synthesis in Liquid of Oxide, Metal-Oxide Core-Shell, and Doped Oxide Nanoparticles. *Chem.—Eur. J.* **2020**, *26*, 9206−9242.

(13) Kabashin, A. V.; Meunier, M. Synthesis of Colloidal Nanoparticle during Femtosecond Laser Ablation of Gold in Water. *J. Appl. Phys.* **2003**, *94*, 7941−7943.

(14) Marzun, G.; Nakamura, J.; Zhang, X.; Barcikowski, S.; Wagener, P. Size Control and Supporting of Palladium Nanoparticles Made by Laser Ablation in Saline Solution as a Facile Route to Heterogeneous Catalysts. *Appl. Surf. Sci.* **2015**, *348*, 75−84.

(15) Shih, C. Y.; Streubel, R.; Heberle, J.; Letzel, A.; Shugaev, M. V.; Wu, C.; Schmidt, M.; Gökce, B.; Barcikowski, S.; Zhigilei, L. V. *Nanoscale* **2018**, *10*, No. 6900.

(16) Shih, C.-Y.; Chen, C.; Rehbock, C.; Tymoczko, A.; Wiedwald, U.; Kamp, M.; Schuermann, U.; Kienle, L.; Barcikowski, S.; Zhigilei, L. V. Limited Elemental Mixing in Nanoparticles Generated by Ultrashort Pulse Laser Ablation of AgCu Bilayer Thin Films in a Liquid Environment: Atomistic Modeling and Experiments. *J. Phys. Chem. C* **2021**, *125*, 2132−2155.

(17) Shih, C.-Y.; Shugaev, M. V.; Wu, C.; Zhigilei, L. V. Generation of Subsurface Voids, Incubation Effect, and Formation of Nanoparticles in Short Pulse Laser Interactions with Bulk Metal Targets in Liquid: Molecular Dynamics Study. *J. Phys. Chem. C* **2017**, *121*, 16549−16567.

(18) Ibrahimkutty, S.; Wagener, P.; Rolo, T. D.; Karpov, D.; Menzel, A.; Baumbach, T.; Barcikowski, S.; Plech, A. A Hierarchical View on

Material Formation during Pulsed-Laser Synthesis of Nanoparticles in Liquid. *Sci. Rep.* **2015**, *5*, No. 16313.
(19) Reich, S.; Letzel, A.; Menzel, A.; Kretzschmar, N.; Gökce, B.; Barcikowski, S.; Plech, A. Early Appearance of Crystalline Nanoparticles in Pulsed Laser Ablation in Liquids Dynamics. *Nanoscale* **2019**, *11*, 6962−6969.
(20) Barcikowski, S.; Plech, A.; Suslick, K. S.; Vogel, A. Materials Synthesis in a Bubble. *MRS Bull.* **2019**, *44*, 382−391.
(21) Takami, A.; Kurita, H.; Koda, S. Laser-Induced Size Reduction of Noble Metal Particles. *J. Phys. Chem. B* **1999**, *103*, 1226−1232.
(22) Amendola, V.; Meneghetti, M. Controlled Size Manipulation of Free Gold Nanoparticles by Laser Irradiation and Their Facile Bioconjugation. *J. Mater. Chem.* **2007**, *17*, 4705−4710.
(23) Hashimoto, S.; Werner, D.; Uwada, T. Studies on the Interaction of Pulsed Lasers with Plasmonic Gold Nanoparticles toward Light Manipulation, Heat Management, and Nanofabrication. *J. Photochem. Photobiol. C* **2012**, *13*, 28−54.
(24) Ziefuß, A. R.; Reichenberger, S.; Rehbock, C.; Chakraborty, I.; Gharib, M.; Parak, W. J.; Barcikowski, S. Laser Fragmentation of Colloidal Gold Nanoparticles with High-Intensity Nanosecond Pulses Is Driven by a Single-Step Fragmentation Mechanism with a Defined Educt Particle-Size Threshold. *J. Phys. Chem. C* **2018**, *122*, No. 22125.
(25) Lau, M.; Haxhiaj, I.; Wagener, P.; Intartaglia, R.; Brandi, F.; Nakamura, J.; Barcikowski, S. Ligand-Free Gold Atom Clusters Adsorbed on Graphene Nano Sheets Generated by Oxidative Laser Fragmentation in Water. *Chem. Phys. Lett.* **2014**, *610*−*611*, 256−260.
(26) Ziefuss, A. R.; Steenbock, T.; Benner, D.; Plech, A.; Göttlicher, J.; Teubner, M.; Grimm-Lebsanft, B.; Rehbock, C.; Comby-Zerbino, C.; Antoine, R.; Amans, D.; Chakraborty, I.; Bester, G.; Nachev, M.; Sures, B.; Rübhausen, M.; Parak, W. J.; Barcikowski, S. Photoluminescence of Fully Inorganic Colloidal Gold Nanocluster and Their Manipulation Using Surface Charge Effects. *Adv. Mater.* **2021**, *33*, No. 2101549.
(27) Spellauge, M.; Tack, M.; Streubel, R.; Miertz, M.; Exner, K. S.; Reichenberger, S.; Barcikowski, S.; Huber, H. P.; Ziefuss, A. R. Photomechanical Laser Fragmentation of IrO_2 Microparticles for the Synthesis of Active and Redox-Sensitive Colloidal Nanoclusters. *Small* **2023**, *19*, No. 2206485.
(28) Pyatenko, A.; Wang, H.; Koshizaki, N.; Tsuji, T. Mechanism of Pulse Laser Interaction with Colloidal Nanoparticles. *Laser Photonics Rev.* **2013**, *7*, 596−604.
(29) Skripov, V. P. In *Metastable Liquids*; Wiley: New York, 1974.
(30) Shugaev, M. V.; He, M.; Levy, Y.; Mazzi, A.; Miotello, A.; Bulgakova, N. M.; Zhigilei, L. V.; Laser-Induced Thermal Processes: Heat Transfer, Generation of Stresses, Melting and Solidification, Vaporization and Phase Explosion, In *Handbook of Laser Micro- and Nano-Engineering*; Sugioka, K.. Eds.; Springer: Cham, Switzerland, 2021, pp 83−163 https://doi.org/10.1007/978-3-030-63647-0_11.
(31) Strasser, M.; Setoura, K.; Langbein, U.; Hashimoto, S. Computational Modeling of Pulsed Laser-Induced Heating and Evaporation of Gold Nanoparticles. *J. Phys. Chem. C* **2014**, *118*, 25748−25755.
(32) Huang, H.; Zhigilei, L. V. Atomistic View of Laser Fragmentation of Nanoparticles in a Liquid Environment. *J. Phys. Chem. C* **2021**, *125*, 13413−13432.
(33) Huang, H.; Zhigilei, L. V. Computational Study of Laser Fragmentation in Liquid: Phase Explosion, Inverse Leidenfrost Effect at the Nanoscale, and Evaporation in a Nanobubble. *Sci. China: Phys. Mech. Astron.* **2022**, *65*, No. 274206.
(34) Inasawa, S.; Sugiyama, M.; Yamaguchi, Y. Bimodal Size Distribution of Gold Nanoparticles under Picosecond Laser Pulses. *J. Phys. Chem. B* **2005**, *109*, 9404−9410.
(35) Werner, D.; Hashimoto, S. Controlling the Pulsed-Laser-Induced Size Reduction of Au and Ag Nanoparticles via Changes in the External Pressure, Laser Intensity, and Excitation Wavelength. *Langmuir* **2013**, *29*, 1295−1302.
(36) Ziefuss, A. R.; Reich, S.; Reichenberger, S.; Levantino, M.; Plech, A. In Situ Structural Kinetics of Picosecond Laser-Induced Heating and Fragmentation of Colloidal Gold Spheres. *Phys. Chem. Chem. Phys.* **2020**, *22*, 4993−5001.
(37) Paltauf, G.; Dyer, P. E. Photomechanical Processes and Effects in Ablation. *Chem. Rev.* **2003**, *103*, 487−518.
(38) Leveugle, E.; Ivanov, D. S.; Zhigilei, L. V. Photomechanical Spallation of Molecular and Metal Targets: Molecular Dynamics Study. *Appl. Phys. A: Mater. Sci. Process.* **2004**, *79*, 1643−1655.
(39) Paltauf, G.; Schmidt-Kloiber, H. Photoacoustic Cavitation in Spherical and Cylindrical Absorbers. *Appl. Phys. A: Mater. Sci. Process.* **1999**, *68*, 525−531.
(40) Zhigilei, L. V.; Garrison, B. J. Computer Simulation Study of Damage and Ablation of Submicron Particles from Short Pulse Laser Irradiation. *Appl. Surf. Sci.* **1998**, *127*−*129*, 142−150.
(41) Zhigilei, L. V.; Garrison, B. J. Microscopic Simulation of Short Pulse Laser Damage of Melanin Particles. *Proc. SPIE* **1998**, *3254*, 135−143.
(42) Schoolcraft, T. A.; Constable, G. S.; Zhigilei, L. V.; Garrison, B. J. Molecular Dynamics Simulation of the Laser Disintegration of Aerosol Particles. *Anal. Chem.* **2000**, *72*, 5143−5150.
(43) Friedenauer, T.; Buck, K.; Eberwein, M.; Bünte, A.-L.; Rehbock, C.; Barcikowski, S. Efficient Formulation of Submicrometer-Sized Active Pharmaceuticals by Laser Fragmentation in a Liquid-Jet Passage Reactor with Minimum Degradation. *Part. Part. Syst. Charact.* **2023**, *40* (12), No. 2300034.
(44) Delfour, L.; Itina, T. E. Mechanisms of Ultrashort Laser-Induced Fragmentation of Metal Nanoparticles in Liquids: Numerical Insights. *J. Phys. Chem. C* **2015**, *119*, 13893−13900.
(45) Fahdiran, R.; Urbassek, H. M. Ultrafast Laser Irradiation of Spherical Nanoparticles: Molecular-Dynamics Results on Fragmentation and Small-Angle Scattering. *Eur. Phys. J. D* **2015**, *69*, No. 35.
(46) Plech, A.; Kotaidis, V.; Lorenc, M.; Boneberg, J. Femtosecond Laser Near-Field Ablation from Gold Nanoparticles. *Nat. Phys.* **2006**, *2*, 44−47.
(47) Voss, J. M.; Olshin, P. K.; Charbonnier, R.; Drabbels, M.; Lorenz, U. J. In Situ Observation of Coulomb Fission of Individual Plasmonic Nanoparticles. *ACS Nano* **2019**, *13*, 12445−12451.
(48) Ihm, Y.; Cho, D. H.; Sung, D.; Nam, D.; Jung, C.; Sato, T.; Kim, S.; Park, J.; Kim, S.; Gallagher-Jones, M.; Kim, Y.; Xu, R.; Owada, S.; Shim, J. H.; Tono, K.; Yabashi, M.; Ishikawa, T.; Miao, J.; Noh, D. Y.; Song, C. Direct Observation of Picosecond Melting and Disintegration of Metallic Nanoparticles. *Nat. Commun.* **2019**, *10*, No. 2411.
(49) Bongiovanni, G.; Olshin, P. K.; Yan, C.; Voss, J. M.; Drabbels, M.; Lorenz, U. J. The Fragmentation Mechanism of Gold Nanoparticles in Water under Femtosecond Laser Irradiation. *Nanoscale Adv.* **2021**, *3*, 5277−5283.
(50) Werner, D.; Furube, A.; Okamoto, T.; Hashimoto, S. Femtosecond Laser-Induced Size Reduction of Aqueous Gold Nanoparticles: In Situ and Pump−Probe Spectroscopy Investigations Revealing Coulomb Explosion. *J. Phys. Chem. C* **2011**, *115*, 8503−8512.
(51) Kotaidis, V.; Plech, A. Cavitation Dynamics on the Nanoscale. *Appl. Phys. Lett.* **2005**, *87*, No. 213102.
(52) Siems, A.; Weber, S. A. L.; Boneberg, J.; Plech, A. Thermodynamics of Nanosecond Nanobubble Formation at Laser-Excited Metal Nanoparticles. *New J. Phys.* **2011**, *13*, No. 043018.
(53) Plech, A.; Ibrahimkutty, S.; Reich, S.; Newby, G. Thermal Dynamics of Pulsed-Laser Excited Gold Nanorods in Suspension. *Nanoscale* **2017**, *9*, 17284−17292.
(54) Lapotko, D. Optical Excitation and Detection of Vapor Bubbles around Plasmonic Nanoparticles. *Opt. Express* **2009**, *17*, 2538−2556.
(55) Katayama, T.; Setoura, K.; Werner, D.; Miyasaka, H.; Hashimoto, S. Picosecond-to-Nanosecond Dynamics of Plasmonic Nanobubbles from Pump-Probe Spectral Measurements of Aqueous Colloidal Gold Nanoparticles. *Langmuir* **2014**, *30*, 9504−9513.
(56) Tabayashi, Y.; Sakaki, S.; Koshizaki, N.; Yamauchi, Y.; Ishikawa, Y. Behavior of Thermally Induced Nanobubbles during Instantaneous Particle Heating by Pulsed Laser Melting in Liquid. *Langmuir* **2021**, *37*, 7167−7175.

(57) Zheng, Y.; Zhong, X.; Li, Z.; Xia, Y. Successive, Seed-Mediated Growth for the Synthesis of Single-Crystal Gold Nanospheres with Uniform Diameters Controlled in the Range of 5−150 nm. *Part. Part. Syst. Charact.* **2014**, *31*, 266−273.
(58) Ziefuß, A. R.; Barcikowski, S.; Rehbock, C. Synergism between Specific Halide Anions and pH Effects during Nanosecond Laser Fragmentation of Ligand-Free Gold Nanoparticles. *Langmuir* **2019**, *35*, 6630−6639.
(59) Hartland, G. V. Review of Electron-Phonon Coupling and Heat Dissipation in Metal Nanoparticles. *Int. J. Nanotechnol.* **2004**, *1*, 307−327.
(60) Hartland, G. V. Optical Studies of Dynamics in Noble Metal Nanostructures. *Chem. Rev.* **2011**, *111*, 3858−3887.
(61) Hartland, G. V. Coherent Vibrational Motion in Metal Particles: Determination of the Vibrational Amplitude and Excitation Mechanism. *J. Chem. Phys.* **2002**, *116*, 8048−8055.
(62) Kotaidis, V.; Dekorsy, T.; Ibrahimkutty, S.; Issenmann, D.; Khakhulin, D.; Plech, A. Vibrational Symmetry Breaking of Supported Nanospheres. *Phys. Rev. B* **2012**, *86*, No. 100101.
(63) Clark, J. N.; Beitra, L.; Xiong, G.; Higginbotham, A.; Fritz, D. M.; Lemke, H. T.; Zhu, D.; Chollet, M.; Williams, G. J.; Messerschmidt, M.; Abbey, B.; Harder, R. J.; Korsunsky, A. M.; Wark, J. S.; Robinson, I. K. Ultrafast Three-Dimensional Imaging of Lattice Dynamics in Individual Gold Nanocrystals. *Science* **2013**, *341*, 56−59.
(64) Hoeing, D.; Salzwedel, R.; Worbs, L.; Zhuang, Y.; Samanta, A. K.; Lübke, J.; Estillore, A. D.; Dlugolecki, K.; Passow, C.; Erk, B.; Ekanayake, N.; Ramm, D.; Correa, J.; Papadopoulou, C. C.; Noor, A. T.; Schulz, F.; Selig, M.; Knorr, A.; Ayyer, K.; Küpper, J.; Lange, H. Time-Resolved Single-Particle X-ray Scattering Reveals Electron-Density Gradients as Coherent Plasmonic-Nanoparticle-Oscillation Source. *Nano Lett.* **2023**, *23*, 5943−5950.
(65) Guzelturk, B.; Utterback, J. K.; Coropceanu, I.; Kamysbayev, V.; Janke, E. M.; Zajac, M.; Yazdani, N.; Cotts, B. L.; Park, S.; Sood, A.; Lin, M.-F.; Reid, A. H.; Kozina, M. E.; Shen, X.; Weathersby, S. P.; Wood, V.; Salleo, A.; Wang, X.; Talapin, D. V.; Ginsberg, N. S.; Lindenberg, A. M. Nonequilibrium Thermodynamics of Colloidal Gold Nanocrystals Monitored by Ultrafast Electron Diffraction and Optical Scattering Microscopy. *ACS Nano* **2020**, *14*, 4792−4804.
(66) Wilson, O. M.; Hu, X.; Cahill, D. G.; Braun, P. V. Colloidal Metal Particles as Probes of Nanoscale Thermal Transport in Fluids. *Phys. Rev. B* **2002**, *66*, No. 224301.
(67) Plech, A.; Kotaidis, V.; Grésillon, S.; Dahmen, C.; von Plessen, G. Laser-Induced Heating and Melting of Gold Nanoparticles Studied by Time-Resolved X-ray Scattering. *Phys. Rev. B* **2004**, *70*, No. 195423.
(68) Plech, A.; Ziefuß, A. R.; Levantino, M.; Streubel, R.; Reich, S.; Reichenberger, S. Low Efficiency of Laser Heating of Gold Particles at the Plasmon Resonance: An X-ray Calorimetry Study. *ACS Photonics* **2022**, *9*, 2981−2990.
(69) Arbouet, A.; Voisin, C.; Christofilos, D.; Langot, P.; Del Fatti, N.; Vallée, F.; Lermé, J.; Celep, G.; Cottancin, E.; Gaudry, M.; Pellarin, M.; Broyer, M.; Maillard, M.; Pileni, M. P.; Treguer, M. Electron-Phonon Scattering in Metal Clusters. *Phys. Rev. Lett.* **2003**, *90*, No. 177401.
(70) Mongin, D.; Maioli, P.; Burgin, J.; Langot, P.; Cottancin, E.; D'Addato, S.; Canut, B.; Treguer, M.; Crut, A.; Vallée, F.; Del Fatti, N. Ultrafast Electron-Lattice Thermalization in Copper and Other Noble Metal Nanoparticles. *J. Phys.: Condens. Matter* **2019**, *31*, No. 084001.
(71) Arblaster, J. W. Thermodynamic Properties of Gold. *J. Phase Equilibria Diffus.* **2016**, *37*, 229−245.
(72) Touloukian, Y. S.; Kirby, R. K.; Taylor, R. E.; Desai, P. D.; Thermal Expansion: Metallic Elements and Alloys. In *Thermophysical Properties of Matter*; IFI Plenum: New York, 1975; Vol. *12*.
(73) Pamato, M. G.; Wood, I. G.; Dobson, D. P.; Hunt, S. A.; Vočadlo, L. The Thermal Expansion of Gold: Point Defect Concentrations and Pre-Melting in a Face-Centered Cubic Metal. *J. Appl. Crystallogr.* **2018**, *51*, 470−480.
(74) The NP size dependence of the melting temperature[75] is neglected in the analysis, as the melting temperature depression is estimated to be relatively small for NP sizes considered in the present study. In particular, for a CTAB NP with a diameter of 44 nm, the Gibbs−Thomson equation yields the melting temperature of 1310 K, which is only 2% below the bulk value of T_m = 1337 K.
(75) Buffat, P.; Borel, J.-P. Size Effect on the Melting Temperature of Gold Particles. *Phys. Rev. A* **1976**, *13*, 2287−2298.
(76) The contribution of surface energy of NPs is neglected in the analysis, as it does not significantly contribute to the overall energy balance. For a 44 nm NP and experimental surface energies of solid and liquid Au, 1.41 and 1.14 J/m^2, respectively,[77] the surface contributes ∼0.02 eV/atom to the energy density of the NP.
(77) Howe, J. M.; In *Interfaces in Materials: Atomic Structure, Thermodynamics and Kinetics of Solid-Vapor, Solid-Liquid and Solid-Solid Interfaces*; Wiley: New York, 1997.
(78) Arefev, M. I.; Shugaev, M. V.; Zhigilei, L. V. Kinetics of Laser-Induced Melting of Thin Gold Film: How Slow Can It Get? *Sci. Adv.* **2022**, *8*, No. eabo2621.
(79) Luo, S.-N.; Ahrens, T. J.; Çağın, T.; Strachan, A.; Goddard, W. A., III; Swift, D. C. Maximum Superheating and Undercooling: Systematics, Molecular Dynamics Simulations, and Dynamic Experiments. *Phys. Rev. B* **2003**, *68*, No. 134206.
(80) Kikhney, A. G.; Svergun, D. I. A; Practical Guide to Small Angle X-ray Scattering (SAXS) of Flexible and Intrinsically Disordered Proteins. *FEBS Lett.* **2015**, *589*, 2570−2577.
(81) Guinier, A. *X-ray Diffraction in Crystals, Imperfect Crystals, and Amorphous Bodies*; W. H. Freeman and Company: San Francisco and London, 1994.
(82) Swiatkowska-Warkocka, Z.; Pyatenko, A.; Koga, K.; Kawaguchi, K.; Wang, H.; Koshizaki, N. Various Morphologies/Phases of Gold-Based Nanocomposite Particles Produced by Pulsed Laser Irradiation in Liquid Media: Insight into Physical Processes Involved in Particle Formation. *J. Phys. Chem. C* **2017**, *121*, 8177−8187.
(83) Streubel, R.; Barcikowski, S.; Gökce, B. Continuous Multigram Nanoparticle Synthesis by High-Power, High-Repetition-Rate Ultrafast Laser Ablation in Liquids. *Opt. Lett.* **2016**, *41*, 1486−1489.
(84) Waag, F.; Streubel, R.; Gökce, B.; Barcikowski, S. Synthesis of Gold, Platinum, and Gold-Platinum Alloy Nanoparticle Colloids with High-Power Megahertz-Repetition-Rate Lasers: The Importance of the Beam Guidance Method. *Appl. Nanosci.* **2021**, *11*, 1303−1312.
(85) Werner, D.; Hashimoto, S.; Uwada, T. Remarkable Photothermal Effect of Interband Excitation on Nanosecond Laser-Induced Reshaping and Size Reduction of Pseudospherical Gold Nanoparticles in Aqueous Solution. *Langmuir* **2010**, *26*, 9956−9963.
(86) Magnozzi, M.; Proietti Zaccaria, R.; Catone, D.; O'Keeffe, P.; Paladini, A.; Toschi, F.; Alabastri, A.; Canepa, M.; Bisio, F. Interband Transitions Are More Efficient Than Plasmonic Excitation in the Ultrafast Melting of Electromagnetically Coupled Au Nanoparticles. *J. Phys. Chem. C* **2019**, *123*, 16943−16950.
(87) Chen, C.; Zhigilei, L. V. Atomistic Modeling of Pulsed Laser Ablation in Liquid: Spatially and Time-Resolved Maps of Transient Nonequilibrium States and Channels of Nanoparticle Formation. *Appl. Phys. A: Mater. Sci. Process.* **2023**, *129*, No. 288.
(88) Zerebecki, S.; Reichenberger, S.; Barcikowski, S. Continuous-Flow Flat Jet Setup for Uniform Pulsed Laser Postprocessing of Colloids. *J. Phys. Chem. A* **2020**, *124*, 11125−11132.
(89) Plech, A.; Kotaidis, V.; Lorenc, M.; Wulff, M. Thermal Dynamics in Laser Excited Metal Nanoparticles. *Chem. Phys. Lett.* **2005**, *401*, 565−569.
(90) Jankowski, M.; Belova, V.; Chushkin, Y.; Zontone, F.; Levantino, M.; Narayanan, T.; Konovalov, O.; Pastore, A. The Complex Systems and Biomedical Sciences Group at the ESRF: Current Status and New Opportunities after Extremely Brilliant Source Upgrade. *Nucl. Instr. Meth. Phys. Res. B* **2023**, *538*, 164−172.
(91) Warren, B. E.; *X-ray Diffraction*; Dover Publications: New York, 1990.
(92) Taché, O.; Spalla, O.; Thill, A.; Carriere, D.; Testard, F.; Sen, D. pySAXS, an Open Source Python Package and GUI for SAXS Data

Treatment, 2013−2022, https://iramis.cea.fr/en/Phocea/Vie_des_labos/Ast/ast_sstechnique.php?id_ast=1799.
(93) Beaucage, G. Approximations Leading to a Unified Exponential/Power-Law Approach to Small-Angle Scattering. *J. Appl. Crystallogr.* **1995**, *28*, 717−728.
(94) Ivanov, D. S.; Zhigilei, L. V. Combined Atomistic-Continuum Modeling of Short-Pulse Laser Melting and Disintegration of Metal Films. *Phys. Rev. B* **2003**, *68*, No. 064114.
(95) Wu, C.; Zhigilei, L. V. Microscopic Mechanisms of Laser Spallation and Ablation of Metal Targets from Large-Scale Molecular Dynamics Simulations. *Appl. Phys. A: Mater. Sci. Process.* **2014**, *114*, 11−32.
(96) Zhou, M.; Zeng, C.; Chen, Y.; Zhao, S.; Sfeir, M. Y.; Zhu, M.; Jin, R. Evolution from the Plasmon to Exciton State in Ligand-Protected Atomically Precise Gold Nanoparticles. *Nat. Commun.* **2016**, *7*, No. 13240.
(97) Zhakhovskii, V. V.; Inogamov, N. A.; Petrov, Y. V.; Ashitkov, S. I.; Nishihara, K. Molecular Dynamics Simulation of Femtosecond Ablation and Spallation with Different Interatomic Potentials. *Appl. Surf. Sci.* **2009**, *255*, 9592−9596.
(98) Tabetah, M.; Matei, A.; Constantinescu, C.; Mortensen, N. P.; Dinescu, M.; Schou, J.; Zhigilei, L. V. The Minimum Amount of "Matrix" Needed for Matrix-Assisted Pulsed Laser Deposition of Biomolecules. *J. Phys. Chem. B* **2014**, *118*, 13290−13299.
(99) Shih, C.-Y.; Wu, C.; Shugaev, M. V.; Zhigilei, L. V. Atomistic Modeling of Nanoparticle Generation in Short Pulse Laser Ablation of Thin Metal Films in Water. *J. Colloid Interface Sci.* **2017**, *489*, 3−17.
(100) Karim, E. T.; Shugaev, M. V.; Wu, C.; Lin, Z.; Hainsey, R. F.; Zhigilei, L. V. Atomistic Simulation Study of Short Pulse Laser Interactions with a Metal Target under Conditions of Spatial Confinement by a Transparent Overlayer. *J. Appl. Phys.* **2014**, *115*, No. 183501.
(101) Shugaev, M. V.; Gnilitskyi, I.; Bulgakova, N. M.; Zhigilei, L. V. Mechanism of Single-Pulse Ablative Generation of Laser-Induced Periodic Surface Structures. *Phys. Rev. B* **2017**, *96*, No. 205429.
(102) Lin, Z.; Zhigilei, L. V. Time-Resolved Diffraction Profiles and Atomic Dynamics in Short-Pulse Laser-Induced Structural Transformations: Molecular Dynamics Study. *Phys. Rev. B* **2006**, *73*, No. 184113.

https://doi.org/10.1021/acsnano.3c12314
ACS Nano 2024, 18, 10527−10541